Human Skeletal Muscle Fiber Heterogeneity Beyond Myosin Heavy Chains

Roger Moreno-Justicia[1]*, Thibaux Van der Stede[2,3]*, Ben Stocks[1]*, Jenni Laitila[4], Robert A Seaborne[4,5], Alexia Van de Loock[2], Eline Lievens[2], Diana Samodova[1], Leyre Marín-Arraiza[6], Oksana Dmytriyeva[1], Kim Van Vossel[2], Nurten Yigit[7], Jasper Anckaert[7], Anneleen Weyns[2], Ruud Van Thienen[2], Ronni E Sahl[4], Edmar Zanoteli[8], Michael W Lawlor[9,10] , Michael Wierer[11], Pieter Mestdagh[7], Jo Vandesompele[7], Julien Ochala[4], Morten Hostrup[3], Wim Derave[2#], & Atul S Deshmukh[1#]

*Joint first-authors

[#]Co-corresponding authors (Atul S Deshmukh: atul.deshmukh@sund.ku.dk; Wim Derave: wim.derave@ugent.be)

[1]Novo Nordisk Foundation Center for Basic Metabolic Research, Faculty of Health and Medical Sciences, University of Copenhagen, Copenhagen, Denmark

[2]Department of Movement and Sports Sciences, Faculty of Medicine and Health Sciences, Ghent University, Ghent, Belgium

[3]The August Krogh Section for Human Physiology, Department of Nutrition, Exercise and Sports, University of Copenhagen, Copenhagen, Denmark

[4]Department of Biomedical Sciences, Faculty of Health and Medical Sciences, University of Copenhagen, Copenhagen, Denmark

[5]Centre for Human and Applied Physiological Sciences, King's College London, London, United Kingdom (present address).

[6]Novo Nordisk Foundation Center for Protein Research, Faculty of Health and Medical Sciences, University of Copenhagen, Copenhagen, Denmark

[7]Department of Biomolecular Medicine, Faculty of Medicine and Health Sciences, Ghent University, Ghent, Belgium

[8]Department of Neurology, Faculdade de Medicina (FMUSP), Universidade de São Paulo, São Paulo, Brazil

[9]Department of Pathology, Medical College of Wisconsin, Milwaukee, WI, USA

[10]Diverge Translational Science Laboratory, Milwaukee, WI, USA

[11]Proteomics Research Infrastructure, Faculty of Health and Medical Sciences, University of Copenhagen, Copenhagen, Denmark

32 **Graphical Abstract**

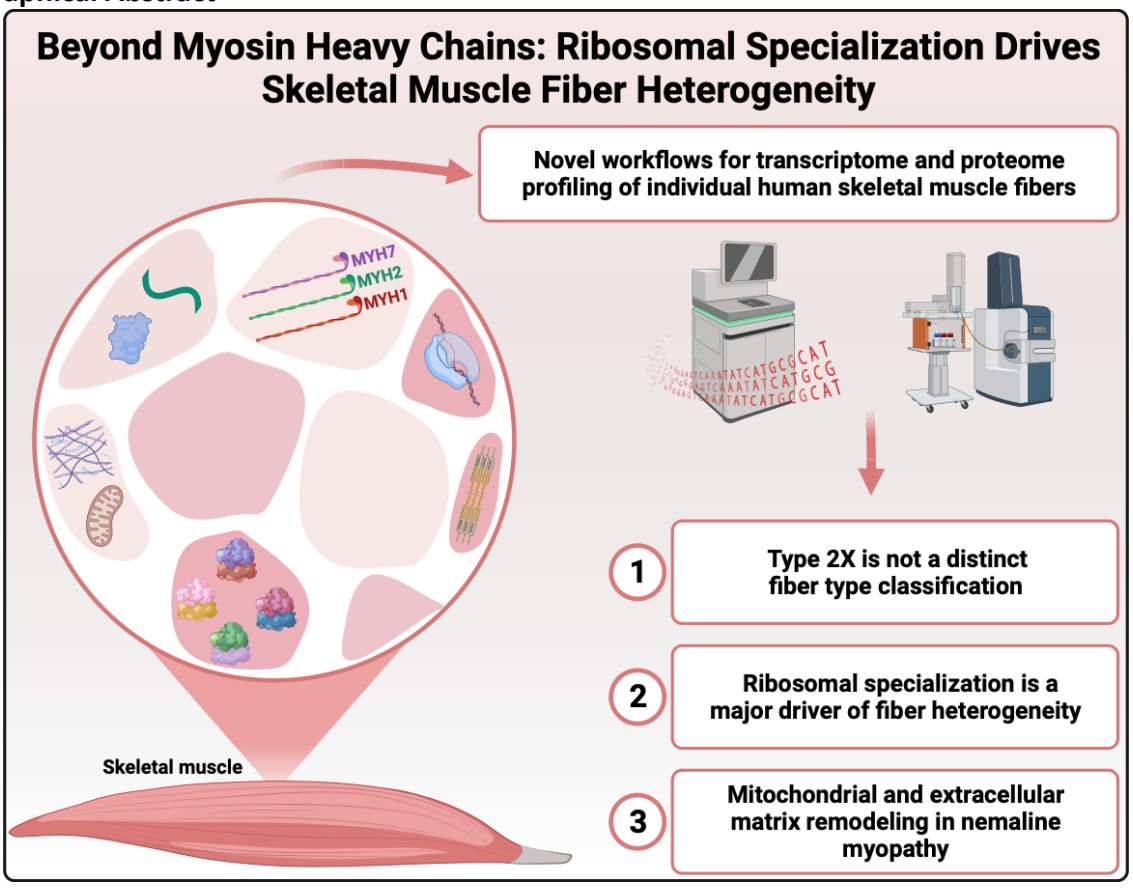

33

Abstract

Skeletal muscle is an inherently heterogenous tissue comprised primarily of myofibers, which are historically classified into three distinct fiber types in humans: one “slow” (type 1) and two “fast” (type 2A and type 2X), delineated by the expression of myosin heavy chain isoforms (MYHs)[1]. However, whether discrete fiber types exist or whether fiber heterogeneity reflects a continuum remains unclear. Furthermore, whether MYHs are the main classifiers of skeletal muscle fibers has not been examined in an unbiased manner. Through the development and application of novel transcriptomic and proteomic workflows, applied to 1050 and 1038 single muscle fibers from human *vastus lateralis*, respectively, we show that MYHs are not the principal drivers of skeletal muscle fiber heterogeneity. Instead, ribosomal heterogeneity and cell junction proteins drive the majority of variance between skeletal muscle fibers in a continual fashion, independent of slow/fast fiber type. Furthermore, whilst slow and fast fiber clusters can be identified, described by their contractile and metabolic profiles, our data challenge the concept that type 2X are phenotypically distinct to other fast fibers at an omics level. Moreover, MYH-based classifications do not adequately describe the phenotype of skeletal muscle fibers in one of the most common genetic muscle diseases, nemaline myopathy, with fibers shifting towards a non-oxidative phenotype independently of MYH-based fiber type. Instead, we characterize novel transcriptomic and proteomic features of slow and fast skeletal muscle fibers, including identifying several muscle fiber type-specific polypeptides, termed microproteins, encoded by transcripts annotated as non-coding RNA. Overall, our data challenges the currently accepted model of multiple distinct fiber types defined by the expression of specific MYHs, and proposes new avenues for skeletal muscle research.

59 **Main**

60 Cellular heterogeneity is an inherent feature of all biological systems, allowing for cellular
61 specialization to meet the diverse demands imposed upon tissues and cells[2]. The classic view
62 of skeletal muscle fiber heterogeneity is that motoneurons define the typology of the fibers
63 within a motor unit, with fiber types being defined by myosin heavy chain isoform (MYH)
64 characteristics[1]. This was first based on its ATPase pH lability[3,4] and later by its molecular MYH
65 expression[5]. Nonetheless, debate continues as to whether discrete fiber types exist (i.e. type
66 1, type 2a, and type 2x in humans) or whether fiber heterogeneity is better described as a
67 continuum[1]. Furthermore, the current view of MYHs as primary classifiers of muscle fibers
68 might be limited and heavily biased by early studies in rodents, displaying a different MYH
69 expression profile and thus fiber type range than humans[1]. This debate has been further
70 fueled by other limitations such as the identification and subsequent acceptance of the
71 existence of "hybrid" fibers that express varying proportions of multiple MYHs simultaneously.
72

73 An unbiased exploration of skeletal muscle fiber diversity with powerful omics tools is thus
74 heavily warranted, but challenging, in part owing to the multinucleated nature of skeletal
75 muscle fibers. Nonetheless, both transcriptomics[6,7] and proteomics[8] technologies have
76 recently experienced a sensitivity revolution due to various technological advances, making
77 profiling of skeletal muscle at a single fiber resolution now possible. As a result, notable
78 progress has already been made in describing the single muscle fiber diversity and responses
79 to atrophic stimuli and aging[9-16]. Importantly, these technological advances lend themselves
80 to being advantageous in the clinical setting, helping to describe in greater detail and precision
81 the dysregulation associated with disease. For example, the underlying pathophysiology of
82 nemaline myopathy, one of the most prevalent genetic muscle disorder (MIM 605355 and
83 MIM 161800), is complex and convoluted[17,18], thus a deeper characterization of skeletal
84 muscle fiber dysregulation may spur significant developments in our understanding of the
85 disease.
86

87 Here, our further methodological development of transcriptome and proteome profiling of
88 single skeletal muscle fibers manually isolated from human biopsy specimens, and their
89 application to over a thousand fibers each, enabled us to investigate the true cellular
90 heterogeneity of human skeletal muscle fibers. In doing so, we demonstrate the power of

91 muscle fiber phenotyping at the transcriptomic and proteomic level, identifying that
92 ribosomal heterogeneity is one of the primary sources of variation among muscle fibers.
93 Furthermore, with our proteomics workflow we characterize the clinical implications of
94 nemaline myopathies within single skeletal muscle fibers, revealing a coordinated shift
95 towards non-oxidative fibers independently of MYH-based fiber type.
96
97 **Results**
98
99 *Development of high-sensitivity and high-throughput single muscle fiber transcriptomic and*
100 *proteomic pipelines*
101
102 To investigate the heterogeneity of human skeletal muscle fibers, we developed two novel
103 workflows to enable transcriptome and proteome profiling of single skeletal muscle fibers (**Fig**
104 **1A and 1 S1A**). Several methodological steps were developed and optimized, from sample
105 storage and preservation of RNA and protein integrity to optimizing the throughput of each
106 method. This was achieved for transcriptome analysis by inserting sample-specific molecular
107 barcodes during the initial reverse transcription step, enabling pooling of 96 fibers for further
108 efficient downstream processing. Rich transcriptome data was further obtained by deeper
109 sequencing (± 1M reads per fiber) compared to conventional single cell methods[19]. For
110 proteomics, the combination of a short chromatographic gradient (21 minutes) and timsTOF
111 DIA-PASEF-based mass spectrometry was used to optimize proteome depth, whilst
112 maintaining a high-throughput[20,21]. To investigate skeletal muscle fiber heterogeneity in the
113 healthy state, the transcriptome was determined for 1050 individual fibers from 14 healthy
114 adult donors, whilst the proteome was determined for 1038 fibers from 5 healthy adult donors
115 (**Table S1)**. These datasets will be referred to as the 1000 fiber transcriptome and proteome
116 datasets, respectively, throughout this manuscript. Our approach detected a total of 27237
117 transcripts and 2983 proteins in the 1000 fiber transcriptomics and proteomics studies (**Fig**
118 **1A, Table S2-3**). After filtering for >1000 detected genes and for 50% valid values within each
119 fiber in both transcriptomics and proteomics datasets, respectively, downstream
120 bioinformatic analyses were performed on 925 and 974 fibers in the transcriptome and
121 proteome, respectively. On average 4257 ± 1557 genes and 2015 ± 234 proteins (mean ± SD)
122 were detected per fiber after filtering, with limited inter-individual variation (**Fig 1 S1B-C,**

123 **Table S4-5**). The intra-individual variation within a participant was more substantial however,
124 most likely due to differences in RNA/protein yield among fibers of different length and cross-
125 sectional area. For the majority of proteins (>2000), the coefficient of variation was below 20%
126 (**Fig 1 S1D**). Both methodologies captured a wide dynamic range of transcripts and proteins,
127 with features known to be important for muscle contraction being highly expressed (e.g.
128 ACTA1, MYH2, MYH7, TNNT1, TNNT3) (**Fig 1 S1E-F**). A large part of the detected features was
129 shared between the transcriptome and proteome datasets (**Fig 1 S1G**), alongside a reasonable
130 correlation (r = 0.52) in average UMI counts/LFQ intensities for these features (**Fig 1 S1H**).
131
132 *Type 2X is not a distinct fiber type*
133
134 We initially set out to define the MYH-based fiber type of each fiber using an optimized
135 methodology, leveraging the high sensitivity and dynamic range of MYH expression in the
136 omics datasets. Previous studies have used arbitrary cut-offs to assign a fiber as pure type 1,
137 type 2A, type 2X, or hybrid, based on a fixed percentage of expression for the different
138 MYHs[9,12,22]. We employed a different approach, in which we ranked the expression of each
139 fiber by the MYHs used for fiber typing: MYH7, MYH2 and MYH1, corresponding to type 1,
140 type 2A and type 2X fibers, respectively. We then mathematically calculated the bottom knee
141 for each of the resulting curves and used it as a threshold to assign a fiber as being positive
142 (above threshold) or negative (below threshold) for each MYH (**Fig 1B-D**). These data show
143 that MYH7 (**Fig 1B**) and MYH2 (**Fig 1C**) have a more pronounced on/off expression profile on
144 the RNA level, compared to the protein level. Indeed, at the protein level, very few fibers did
145 not express MYH7 and no fibers had 100% MYH2 expression. Next, we used the determined
146 expression thresholds to assign MYH-based fiber types for all fibers in each dataset. For
147 example, a $MYH7^{+}/MYH2^{-}/MYH1^{-}$ was assigned as type 1, and a $MYH7^{-}/MYH2^{+}/MYH1^{+}$ was
148 assigned as a hybrid type 2A/2X fiber (see **Table S6** for full description). When combining all
149 fibers, a very similar MYH-based fiber type distribution was observed at the RNA (**Fig 1E**) and
150 protein (**Fig 1F**) levels, with an expected inter-individual variation in relative MYH-based fiber
151 type composition (**Fig 1 S2A**). Most fibers were considered pure type 1 (34-35%) or type 2A
152 (36-38%), although a substantial number of hybrid 2A/2X fibers (16-19%) were also detected.
153 A striking discrepancy was that pure type 2X fibers could only be detected at the RNA but not

at the protein level, indicating that fast MYH expression is, at least in part, post-transcriptionally regulated.

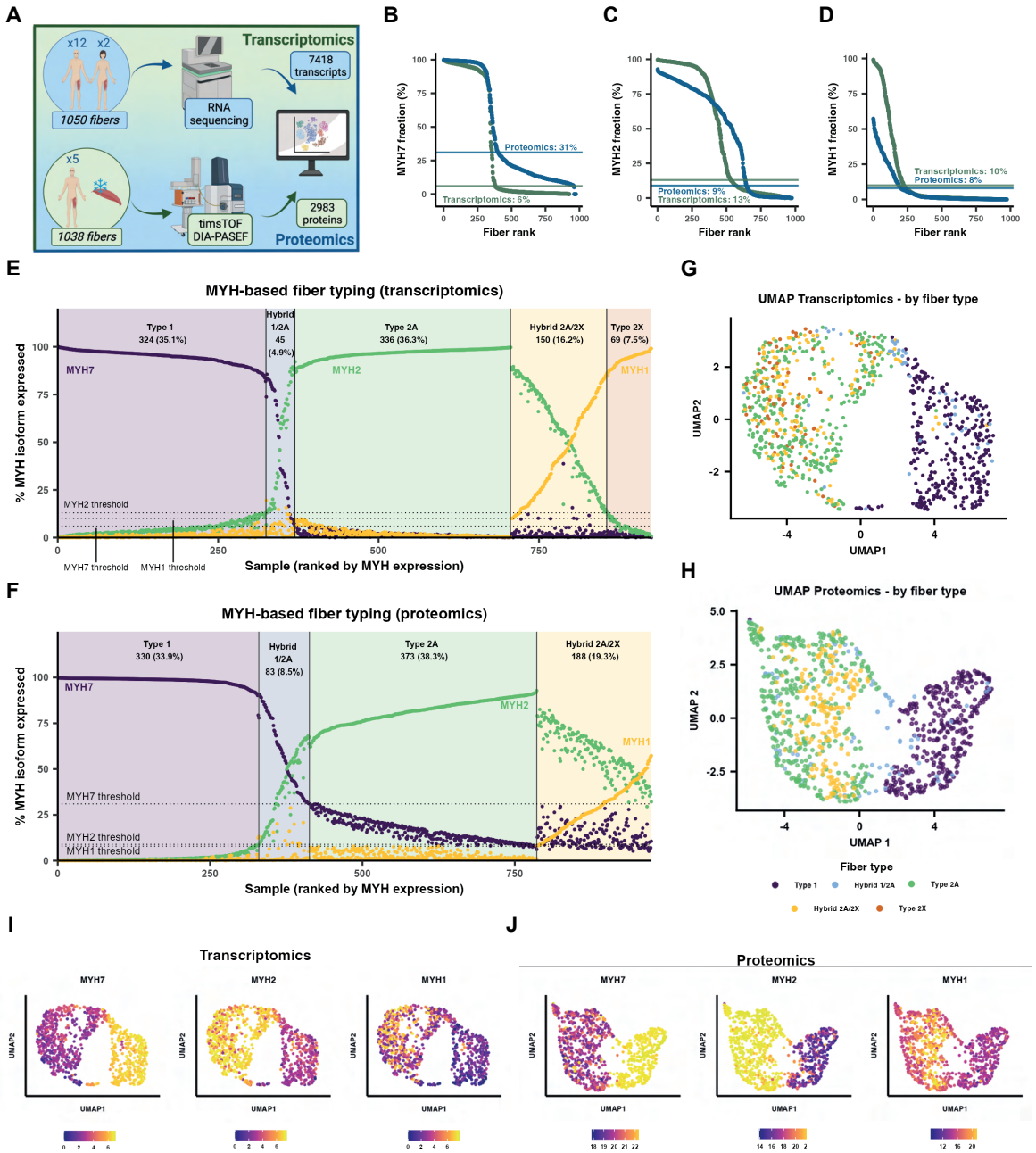

Figure 1. Transcriptomic- and proteomic-based clustering reveals only two distinct fiber types. (A) Transcriptomic and proteomic workflow. **(B-D)** Dynamic range curves for MYH7, MYH2, and MYH1, with calculated assignment thresholds. **(E-F)** Distribution of fibers by expression of MYHs in transcriptomics and proteomics datasets. **(G-H)** Uniform manifold approximation and projection (UMAP) plots for transcriptomics and proteomics, colored by MYH-based fiber type. **(I-J)** Feature plots displaying the expression of MYH7, MYH2, and MYH1 in transcriptomics and proteomics.

163 We validated the MYH-based fiber typing from the proteomics data against an antibody-based
164 dot blot technique, in which both methodologies were in 100% agreement on the
165 identification of both pure type 1 and type 2A fibers (**Fig 1 S2B**). However, the increased
166 sensitivity of the proteomics-based approach was superior in identifying hybrid fibers and in
167 quantifying the proportion of each MYH within each fiber. These data demonstrate the
168 efficacy of using an unbiased high-sensitivity omics-based approach for the characterization
169 of skeletal muscle fiber types.
170
171 We then utilized the full depth of information that transcriptomics and proteomics provide to
172 classify fibers in an unbiased manner based on their whole transcriptome or proteome. Using
173 uniform manifold approximation and projection (UMAP) for dimension reduction of 6
174 principal components (**Fig 1 S3 A-B**), we were able to visualize the variation in fibers in the
175 transcriptome (**Fig 1G**) and proteome (**Fig 1H**). Interestingly, fibers did not cluster by
176 participant in either the transcriptomics or proteomics datasets (**Fig 1 S3C-D**), nor by test day
177 (**Fig 1 S3E**), indicating that intra-individual variance in skeletal muscle fibers outweighs inter-
178 individual variance. Two distinct clusters were apparent in the UMAP plots, which represented
179 "fast" and "slow" fibers (**Fig 1G-H**). MYH7^{+} (slow) fibers clustered to the positive side of
180 UMAP1, and MYH2^{+} and MYH1^{+} (fast) fibers clustered to the negative side of UMAP1 (**Fig 1I-**
181 **J**). No distinction between the various fast MYH-based fiber types (i.e. type 2A, type 2X, or
182 hybrid 2A/2X) could be identified, however, suggesting that when the whole transcriptome or
183 proteome is taken into account, the expression of MYH1 is not discriminative. Given that we
184 detected no pure 2X fibers at the protein level (**Fig 1F**), these data question the validity of
185 MYH1 as a marker for fiber typing. Furthermore, whilst type 2X fibers can be identified at the
186 transcriptional level based solely on the quantification of MYHs, these fibers cannot be
187 discriminated from other fast fiber types when the whole transcriptome is considered.
188
189 *Considerable skeletal muscle fiber heterogeneity beyond myosin heavy chain isoforms*
190
191 As an initial exploration of fiber heterogeneity beyond MYHs, we assessed four established
192 slow fiber type-specific proteins: TPM3, TNNT1, MYL3, and ATP2A2[1]. In both transcriptomics
193 (**Fig 2 S1A**) and proteomics (**Fig 2 S1B**) approaches, the slow isoforms exhibited a high,
194 although not perfect, Pearson correlation coefficient with MYH7. Approximately 25 and 33%

195 of the fibers in the transcriptomics (**Fig 2 S1C**) and proteomics (**Fig 2 S1D**) approaches,
196 respectively, were not classified as pure slow fibers by all gene/protein isoforms. Thus, fiber
197 typing based on multiple gene/protein isoforms introduces additional complexity, even with
198 well-known proteins that are assumed to be fiber type-specific. This suggests that fiber typing
199 based on isoforms of a single family of genes/proteins is likely inadequate to capture the true
200 heterogeneity of skeletal muscle fibers.
201
202 To further investigate the omics-wide phenotypical variability between human skeletal muscle
203 fibers, we applied unbiased dimensionality reduction by principal component analysis (PCA)
204 to our data (**Fig 2A**). Similarly to the UMAP plot, neither participant nor test day influenced
205 the clustering of fibers at the PCA level (**Fig 2 S2A-C**). MYH-based fiber type was explained by
206 PC2 in both datasets, displaying clusters for slow type 1 fibers and a second cluster containing
207 the fast type 2A, type 2X and hybrid type 2A/2X fibers (**Fig 2A**). These two clusters were
208 bridged in both datasets by a small number of hybrid type 1/2A fibers. As expected, over-
209 representation analysis of the top PC drivers confirmed that PC2 is driven by contractile and
210 metabolic features (**Fig 2B & 2 S2D-E, Table S7-9**). In general, the MYH-based fiber types
211 adequately explain the continual variance along PC2, except for the so-called type 2X fibers,
212 which were spread across the entirety of the transcriptomic fast cluster.
213
214 Unexpectedly, MYH-based fiber type was only the second most important source of variability
215 (PC2), indicating that other biological factors (PC1) independent of MYH-based fiber type,
216 have an even greater role in regulating skeletal muscle fiber heterogeneity. Over-
217 representation analysis of the top drivers in PC1 indicated that variance within PC1 was
218 determined primarily by cell-cell adhesion and ribosomal content in the transcriptome, and
219 costamere and ribosomal proteins in the proteome (**Fig 2B & 2 S2D-E, Table S9**). In skeletal
220 muscle, the costamere connects the Z-disk to the sarcolemma and participates in force
221 transmission and signaling[23]. Annotating PCA plots with cell-cell adhesion (transcriptome, **Fig**
222 **2C**) and costamere (proteome, **Fig 2D**) features showed a strong shift to the left side of PC1,
223 suggesting an enrichment for these features in some fibers.
224
225
226

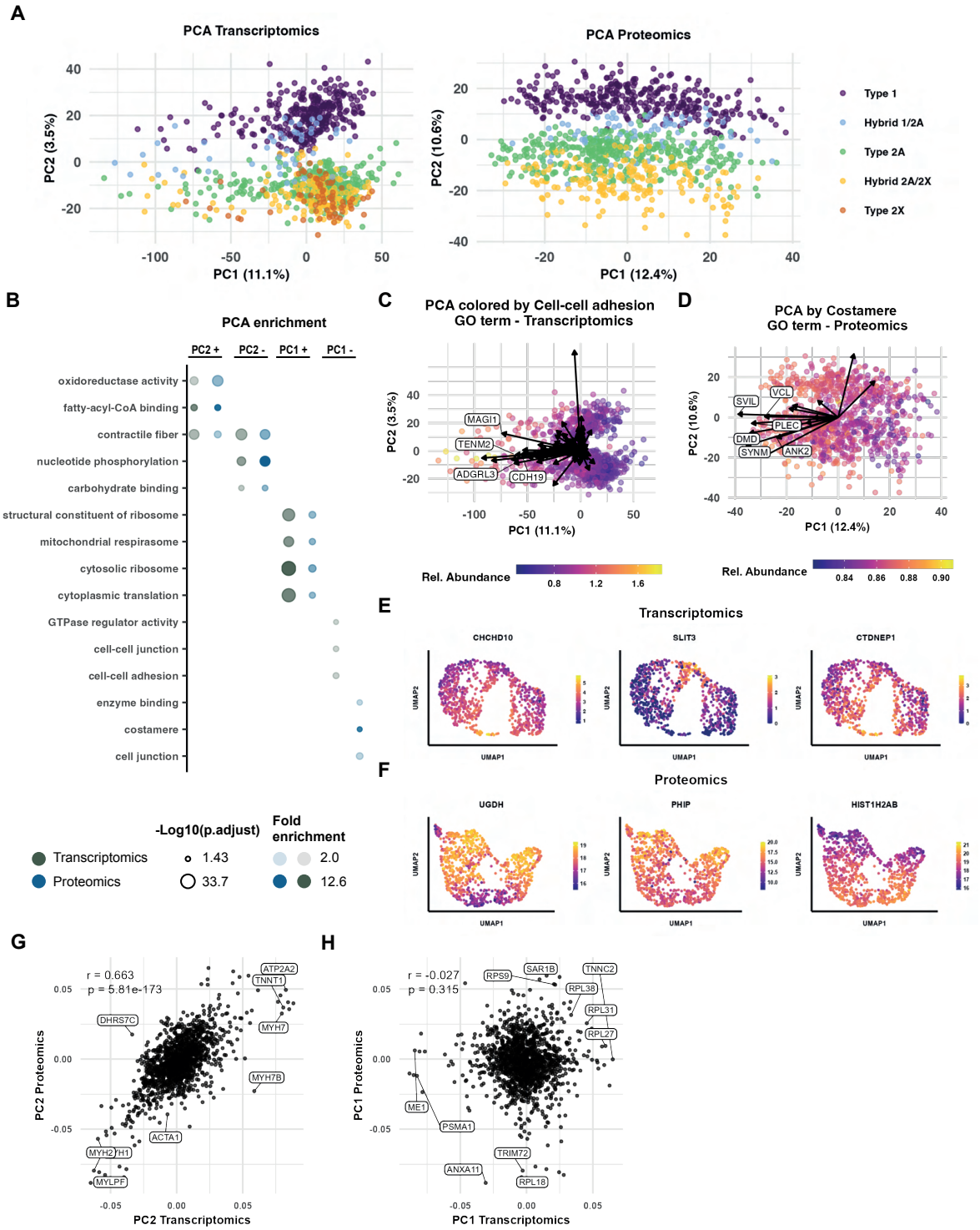

Figure 2. Skeletal muscle fiber heterogeneity beyond MYHs. (A) Principal component analysis (PCA) plots of transcriptomics and proteomics datasets colored by MYH-based fiber type. **(B)** Enrichment analysis of transcript and protein drivers of PC2 and PC1. **(C-D)** PCA plot colored by cell-cell adhesion gene ontology (GO) term in the transcriptome, and by costamere GO term in the proteome. Arrows represent transcript and protein drivers and their direction. **(E-F)** Uniform manifold approximation and projection (UMAP) feature plots of clinically relevant features displaying a slow/fast fiber type-independent gradient of expression. **(G-H)** Correlation between drivers of PC2 and PC1 between the transcriptome and proteome.

234

235 Closer inspection of fiber clustering at the UMAP level showed a MYH-based fiber type-
236 independent gradient of expression for most features, rather than distinct subclusters of
237 muscle fibers. This continuum holds true for several genes related to pathological conditions
238 (**Fig 2E**), such as *CHCHD10* (neuromuscular disorders)[24], *SLIT3* (muscle loss)[25] and *CTDNEP1*
239 (muscle disease)[26]. This same continuum was observed in the proteome, with proteins related
240 to neurological diseases (UGDH)[27], insulin signaling (PHIP)[28] and transcription (HIST1H2AB)
241 (**Fig 2F**). These data collectively show that slow/fast fiber type independent heterogeneity
242 across fibers is of a continual nature, and no distinct subtypes of human skeletal muscle fibers
243 beyond a slow-fast classification should be considered.

244

245 *Fiber heterogeneity is post-transcriptionally regulated by ribosomal heterogeneity*

246

247 Interestingly, drivers of PC2 showed a good correlation (r = 0.663) between the transcriptome
248 and proteome (**Fig 2G**), indicating that the slow and fast fiber types, particularly the contractile
249 and the metabolic profile of skeletal muscle fibers, are transcriptionally regulated. However,
250 there was no correlation between the drivers of PC1 in the transcriptome and the proteome
251 (r = -0.027) (**Fig 2H**). This suggests that slow/fast fiber type-independent variance is for a large
252 part post-transcriptionally regulated. Since PC1 variance was largely explained by ribosomal
253 gene ontology terms and given that ribosomes play a profound and specialized role in the cell
254 by actively participating and influencing protein translation[29], we next set out to explore this
255 unexpected ribosomal heterogeneity.

256

257 We first colored the proteomics PCA plot based on the relative abundance of the proteins
258 within the "cytosolic ribosome" GOCC term (**Fig 3A**). Although the term was enriched on the
259 positive side of PC1, and a slight gradient could be observed accordingly, ribosomal proteins
260 were driving separation in both directions of PC1 (**Fig 3A**). Amongst the ribosomal proteins
261 enriched in the negative direction of PC1 were RPL18, RPS18 and RPS13 (**Fig 3B**), whilst RPL31,
262 RPL35 and RPL38 (**Fig 3C**) were major drivers in the positive direction of PC1. Interestingly,
263 RPL38 and RPS13 are highly expressed in skeletal muscle when compared to other tissues (**Fig**
264 **3 S1A**). These distinct ribosomal signatures across PC1 could not be observed in the
265 transcriptome (**Fig 3 S1B**), indicating that this phenomenon is post-transcriptionally regulated.

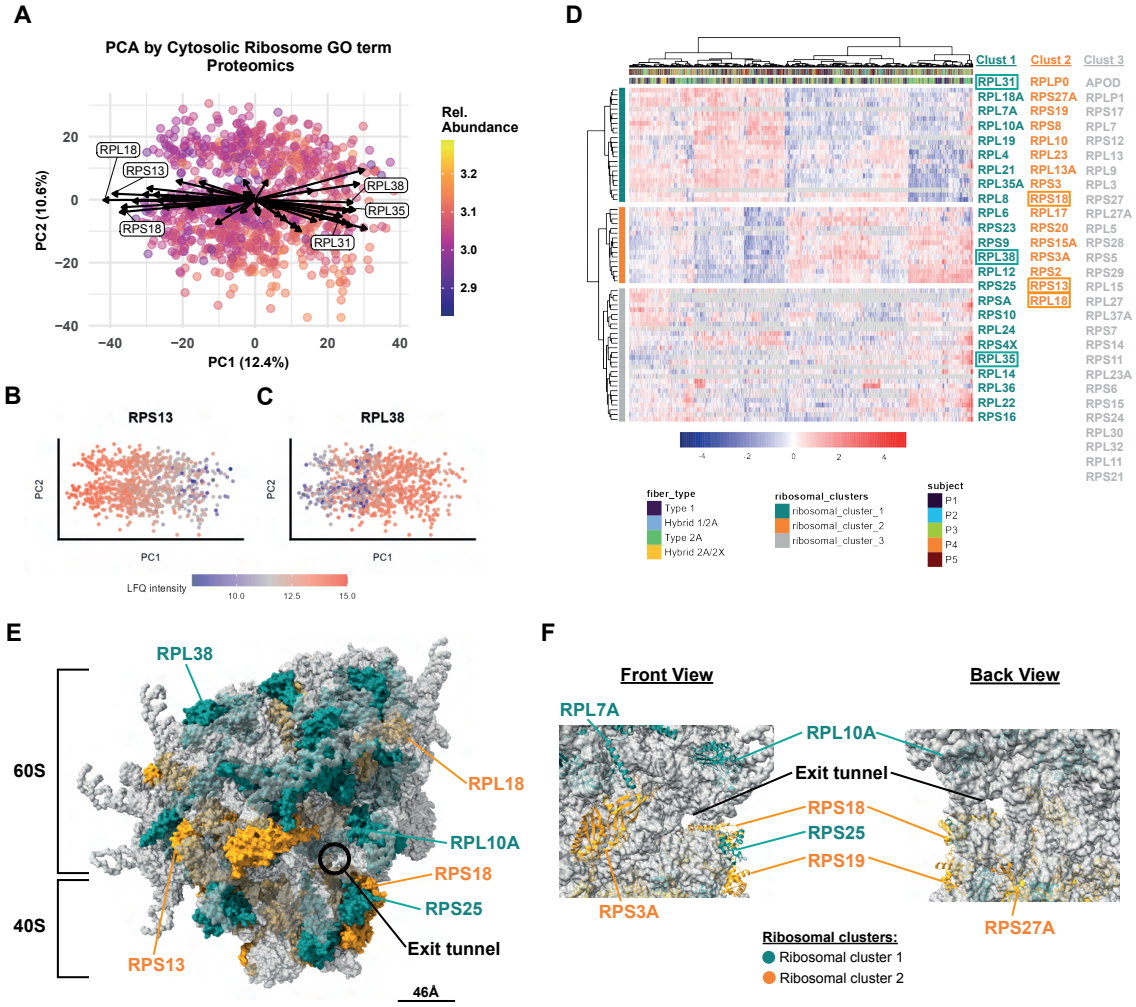

Figure 3. Ribosomal heterogeneity drives fiber type-independent heterogeneity. (A) Principal component analysis (PCA) plot colored by cytosolic ribosome gene ontology (GO) term in the proteome. Arrows represent protein drivers and their direction. **(B-C)** PCA feature plots of RPS13 and RPL38. **(D)** Unsupervised hierarchical clustering analysis of proteins constituting the cytosolic ribosome. **(E)** Structural model of the 80S ribosome (PDB: 4V6X) highlighting ribosomal proteins displaying variable abundance across skeletal muscle fibers. **(F)** Ribosomal proteins with variable stoichiometry located close to the mRNA exit tunnel.

The concept of ribosomal heterogeneity and specialization was previously introduced, where the presence of distinct subpopulations of ribosomes (ribosomal heterogeneity) can directly influence protein translation in different tissues[30] and cells[31] by selectively translating specific mRNA transcript pools[32] (ribosomal specialization). To identify sub-sets of ribosomal proteins that are co-expressed within skeletal muscle fibers, we performed an unsupervised hierarchical clustering analysis of ribosomal proteins within the proteome (**Fig 3D, Table S10**). As expected, ribosomal proteins did not cluster by MYH-based fiber type. However, we identified three distinct clusters of ribosomal proteins; the first of which (ribosomal_cluster_1)

281 was coregulated alongside RPL38, therefore elevated in fibers in the positive direction of PC1.
282 The second cluster (ribosomal_cluster_2) was coregulated alongside RPS13 and was elevated
283 in fibers in the negative direction of PC1. A third cluster (ribosomal_cluster_3) displayed no
284 coordinated differential expression within skeletal muscle fibers and could therefore be
285 considered "core" ribosomal proteins within skeletal muscle. Both ribosomal_cluster_1 and
286 ribosomal_cluster_2 contain ribosomal proteins previously demonstrated to regulate
287 selective translation (e.g. RPL10A, RPL38, RPS19 and RPS25) and functionally influence
288 development (e.g. RPL10A, RPL38)[32-36].
289
290 To visualize the position of the ribosomal proteins that display heterogeneity within the
291 ribosome, we utilized a structural model of the human 80S ribosome (Protein Data Bank:
292 4V6X)[37] (**Fig 3E**). Upon highlighting the ribosomal proteins that belong to the different
293 ribosomal clusters, they were not located in close proximity, showing that our approach did
294 not enrich for a particular area/section of the ribosome. Yet interestingly, ribosomal_cluster_2
295 contained a lower proportion of large ribosomal subunit proteins than ribosomal_cluster_1
296 and ribosomal_cluster_3 (**Fig 3 S1C**). We observed that the majority of the proteins that
297 display variable stoichiometry within skeletal muscle fibers are located on the surface of the
298 ribosome (**Fig 3E**), which is consistent with an ability to interact with internal ribosome entry
299 site (IRES) elements within distinct mRNA populations to coordinate selective translation[38,39].
300 Furthermore, numerous proteins that display variable stoichiometry within skeletal muscle
301 fibers are located close to functional regions, such as the mRNA exit tunnel (**Fig 3F**), which can
302 selectively regulate translation elongation and arrest of specific nascent peptides[40]. Overall,
303 our data identifies that skeletal muscle ribosomal protein stoichiometry displays
304 heterogeneity, driving variance between skeletal muscle fibers.
305
306 *Slow and fast fiber signatures and their transcriptional regulators*
307
308 We next set out to identify novel features of fast and slow skeletal muscle fibers and how
309 these are transcriptionally regulated. Comparing the fast and slow clusters defined in the
310 UMAPs of both datasets (**Fig 1G-H & inlays Fig 4A-B**), transcriptome and proteome analysis
311 yielded 1366 and 804 differentially abundant features, respectively (**Fig 4A-B, Table S11-14**).
312 Expected differences in sarcomeric (e.g. tropomyosin and troponin), excitation-contraction

313 coupling (SERCA isoforms) and energy metabolism-related (e.g. ALDOA and CKB) features
314 were observed. In addition, transcripts and proteins regulating protein ubiquitination
315 displayed differences between fast and slow fibers (e.g. *USP54, SH3RF2,* USP28 and USP48)
316 (**Fig 4A-B**). Furthermore, the microprotein-encoding gene *RP11-451G4.2*, which has
317 previously been shown to be differentially expressed between lamb muscle fiber types[41], was
318 significantly up-regulated in slow skeletal muscle fibers (**Fig 4A**). Also at the single fiber level,
319 clear differences could be observed for known features such as the metabolism-related
320 isoforms of lactate dehydrogenase (LDHA and LDHB, **Fig 4C** and **Fig 4 S1A**)[42,43], as well as
321 previously unknown fiber type-specific features (e.g. *IRX3*, *USP54*, USP28, and DPYSL3) (**Fig**
322 **4C**). There was a reasonable overlap of differentially expressed features (**Fig 4 S1B**) and
323 correlation of fold changes between the transcriptomic and proteomic datasets, primarily
324 driven by the large expression differences in sarcomeric features (**Fig 4 S1C**). Notably, some
325 features (e.g. USP28, USP48, GOLGA4, AKAP13) showed strong post-transcriptional regulation
326 with slow/fast fiber type-specific expression profiles only at the proteome level (**Fig 4 S1B**).
327
328 We next performed over-representation analysis on the differentially abundant genes and
329 proteins (**Fig 4D, Table S15**). Enriched pathways of features that were differential in both
330 datasets showed expected differences such as fatty acid beta-oxidation and ketone metabolic
331 process (slow fibers), myofilament/muscle contraction (fast and slow fibers, respectively) and
332 carbohydrate catabolic process (fast fibers). Serine/Threonine protein phosphatase activity
333 was also enriched in fast fibers, driven by features such as phosphatase regulatory and
334 catalytic subunits (PPP3CB, PPP1R3D, and PPP1R3A), known to regulate glycogen
335 metabolism[44] (**Fig 4 S1D-E**). Other enriched pathways in fast fibers were Processing (P-) bodies
336 (YTHDF3, TRIM21, LSM2) in the proteome (**Fig 4 S1F**), possibly related to post-transcriptional
337 regulation[45], and transcription factor activity (*SREBPF1*, *RXRG*, *RORA*) in the transcriptome (**Fig**
338 **4 S1G**). Slow fibers showed enrichment for oxidoreductase activity (*BDH1*, *DCXR*, *TXN2*) (**Fig 4**
339 **S1H**), amide binding (*CPTP*, *PFDN2*, *CRYAB*) (**Fig 4 S1I**), extracellular matrix (*CTSD*, *ADAMTSL4*,
340 *LAMC1*) (**Fig 4 S1J**) and receptor-ligand activity (*FNDC5*, *SPX*, *NENF*) (**Fig 4 S1K**).

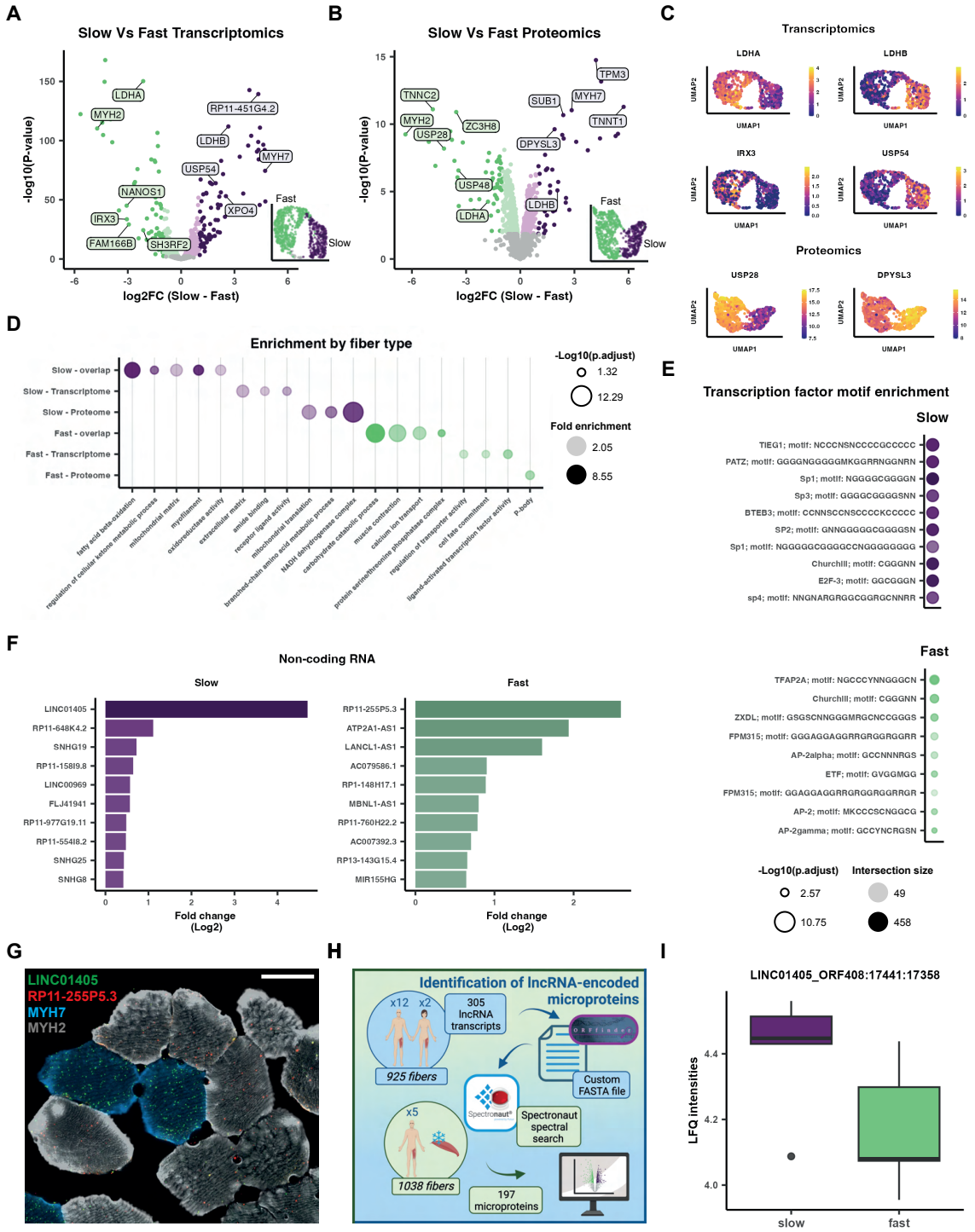

Figure 4. Fast and slow skeletal muscle fiber signatures. (A-B) Volcano plots comparing the slow and fast clusters identified from the uniform manifold approximation and projection (UMAP) plots in Fig 1G-H. Colored dots represent significantly different transcripts or proteins at an FDR < 0.05, darker dots represent significantly different transcripts or proteins with a fold change > 2. (**C**) Feature plots of selected differentially expressed genes or proteins between slow and fast fibers. **(D)** Enrichment analysis of significantly different transcript and proteins. Overlap – enriched in both datasets, Transcriptome – enriched only in transcriptome, Proteome – enriched only in proteome. **(E)** Transcription factor motif enrichment analysis from the transcriptome using the TRANSFAC database. **(F)** Significantly regulated non-coding RNA transcripts. **(G)** Representative RNAscope images displaying

349 the slow/fast fiber-type specificity of LINC01405 and RP11-255P5.3, respectively. Scaling bar = 50 µm. **(H)** De
350 novo microprotein identification workflow. **(I)** The microprotein LINC01405_ORF408:17441:17358 is specific to
351 slow skeletal muscle fibers.
352
353 To get more insights into the transcriptional regulation of slow/fast fiber type signatures, we
354 performed transcription factor binding motif enrichment using the TRANSFAC databases on
355 the differentially expressed genes in the transcriptome dataset (**Table S16**). Many
356 transcription factor binding motifs were significantly enriched between fast and slow fibers
357 (**Fig 4E**). This included known transcription factors such as MEF2[46], enriched in the fast fibers,
358 but also multiple novel transcription factors potentially involved in the fiber type specific gene
359 program. TIEG1, known to regulate mitochondrial content[47], was the most enriched
360 transcription factor within slow fibers and as such should be considered as an important
361 regulator of skeletal muscle metabolism. In addition, PATZ, BTEB3 and multiple motifs from
362 the SP family of transcription factors were enriched in slow muscle fibers. In fast skeletal
363 muscle fibers, TFAP2A, ZXDL, FPM315, AP-2 and ETF are all novel transcription factors
364 putatively regulating skeletal muscle fiber type.
365
366 Alongside known protein-coding genes, there exists a multitude of non-coding RNA biotypes,
367 potentially involved in the regulation of human development and disease[48,49]. Several non-
368 coding RNAs displayed fiber type specificity in the transcriptomics dataset (**Fig 4F & Table S17**),
369 including *LINC01405*, which is very specific to slow fibers and is reported to be downregulated
370 in muscle of mitochondrial myopathy patients[50]. Conversely, *RP11-255P5.3,* corresponding to
371 the *lnc-ERCC5-5* gene (https://lncipedia.org/db/transcript/lnc-ERCC5-5:2)[51] displayed fast
372 fiber type-specificity. Both *LINC01405* (https://tinyurl.com/x5k9wj3h) and *RP11-255P5.3*
373 (https://tinyurl.com/29jmzder) display specificity to skeletal muscle (**Fig 4 S2A-B**) and have
374 very few or no known contractile genes within a 1Mb genomic neighborhood, suggesting a
375 specialized role in fiber type regulation rather than a regulatory role for a neighboring
376 contractile gene. The slow/fast fiber type-specific specific expression profiles of *LINC01405*
377 and *RP11-255P5.3* were independently validated using RNAscope (**Fig 4G**).
378
379 Recently, it has become apparent that numerous assumed non-coding transcripts code for
380 transcribed microproteins, some of which regulate muscle function[52,53]. To identify novel

381 microproteins with potential fiber-type specificity, we searched our 1000 fiber proteomic
382 dataset using a custom FASTA file containing sequences from the detected non-coding
383 transcripts (n = 305) from the 1000 fiber transcriptome dataset (**Fig 4H**). This resulted in the
384 identification of 197 novel microproteins arising from 22 distinct transcripts (**Table S18**, of
385 which 71 microproteins display differential regulation between slow and fast skeletal muscle
386 fibers (**Fig 4 S2C and Table S19**). Three microprotein products were identified for *LINC01405*,
387 of which one displays a slow-fiber type specificity similar to its transcript (**Fig 4I and 4 S2D**).
388 Thus, we identify *LINC01405* as a microprotein-encoding gene, which displays specificity for
389 slow skeletal muscle fibers.
390
391 *Nemaline myopathies induce a shift towards faster, less oxidative skeletal muscle fibers*
392
393 Having developed a comprehensive workflow to characterize the proteome of single muscle
394 fibers at scale and discovered novel regulators of fiber heterogeneity in the healthy state, we
395 applied this pipeline to understand how nemaline myopathy impacts skeletal muscle fiber
396 heterogeneity. Nemaline myopathy is a genetic muscular disorder that causes muscle
397 weakness, resulting in a range of complications for the affected children including respiratory
398 difficulties, scoliosis, and physical immobility[17,18]. Typically, in nemaline myopathy, pathogenic
399 variants in genes such as actin alpha 1 (*ACTA1*) drive the fiber type composition towards slow
400 fiber predominance, although this effect is heterogenous. The only clear exception is the
401 troponin T1 (*TNNT1*) nemaline myopathy, in which a fast fiber predominance is seen. Thus, a
402 deeper characterization of the heterogeneity behind the skeletal muscle fiber dysregulation
403 observed in nemaline myopathies may help untangle the complex relationship between these
404 diseases and muscle fiber types.
405
406 Muscle fibers isolated from patients with *ACTA1*- and *TNNT1*-mutation derived nemaline
407 myopathies display substantial myofiber atrophy or hypotrophy, compared to healthy controls
408 (n = 3 per group) (**Fig 5A, Table S20**), which provides considerable technical challenge arising
409 from the limited material for proteomic analysis. Nonetheless, we were able to detect 2485
410 proteins from 272 skeletal muscle fibers. After filtering for a minimum of 1000 quantified
411 proteins per fiber, downstream bioinformatic analyses were performed on 250 fibers. On
412 average of 1573 ± 359 proteins were quantified per fiber after filtering (**Fig 5 S1A, Table S21-**

413 **22**). Importantly, only a modest reduction in proteome depth was apparent in samples from
414 patients with nemaline myopathy, despite the markedly reduced fiber size. A wide dynamic
415 range was apparent in the proteome, whilst the shared proteins in the control participants
416 correlated well with those in the previous analysis of the 1000 fiber proteome study (**Fig 5**
417 **S1B-C**).
418
419 As nemaline myopathies influence the MYH-based fiber type proportions within skeletal
420 muscle[17,18], we first investigated the MYH-based fiber type of our nemaline myopathy patients
421 and controls. Fiber type was determined using the unbiased approach described previously
422 for the 1000 fiber studies (**Fig 5 S1D-E**) and once again pure type 2X fibers could not be
423 identified (**Fig 5B**). We observed a heterogeneous effect of nemaline myopathies on fiber type
424 two patients with *ACTA1* mutations displaying an increased proportion of type 1 fibers, whilst
425 two patients with *TNNT1*-nemaline myopathy displayed a reduced proportion of type 1 fibers
426 (**Fig 5B**). Indeed, MYH2 and the fast troponin isoforms were downregulated in *ACTA1*-
427 nemaline myopathy (TNNC2, TNNI2, and TNNT3), whilst MYH7 was downregulated in *TNNT1*-
428 neamline myopathy (**Fig 5 S2A**). This is in line with previous reports of heterogeneous fiber
429 type switching in nemaline myopathies[17,18]. We validated these findings using
430 immunohistochemistry, finding type 1 fiber predominance in *ACTA1*-nemaline myopathy
431 patients, while the opposite was observed in *TNNT1-nemaline myopathy* patients (**Fig 5A**).
432
433 At the whole proteome level, skeletal muscle fibers from *ACTA1*- and *TNNT1*-nemaline
434 myopathy patients clustered away from the majority of control fibers, with TNNT1- nemaline
435 myopathy fibers tending to be the most severely affected (**Fig 5C**). This was particularly
436 apparent when we produced a PCA plot of pseudo-bulked fibers for each patient, with *TNNT1*-
437 nemaline myopathy patients 2 & 3 lying furthest from the control samples (**Fig 5 S2B, Table**
438 **S23**). To further understand how fibers from myopathy patients compare to the healthy
439 condition, we capitalized on the depth of information provided by our analysis in 1000 fiber
440 proteome study from healthy adult participants. We projected the fibers from our myopathy
441 data set (both *ACTA1*- and *TNNT1*-nemaline myopathy patients and controls) onto the PCA
442 determined from the 1000 fiber proteome study (**Fig 5D**). Control fibers displayed a similar
443 distribution of MYH-based fiber type along PC2 as the 1000 fiber proteome study. However,
444 the majority of fibers from nemaline myopathy patients shifted downwards along PC2,

445 overlapping with the healthy fast fibers, irrespective of their own MYH-based fiber type. Thus,
446 despite evidence for a fiber-type shift towards type 1 fibers in *ACTA1*-nemaline myopathy
447 patients when quantified using MYH-based approaches, both *ACTA1*- and *TNNT1*-nemaline
448 myopathies shift the skeletal muscle fiber proteome to resemble fast fibers.

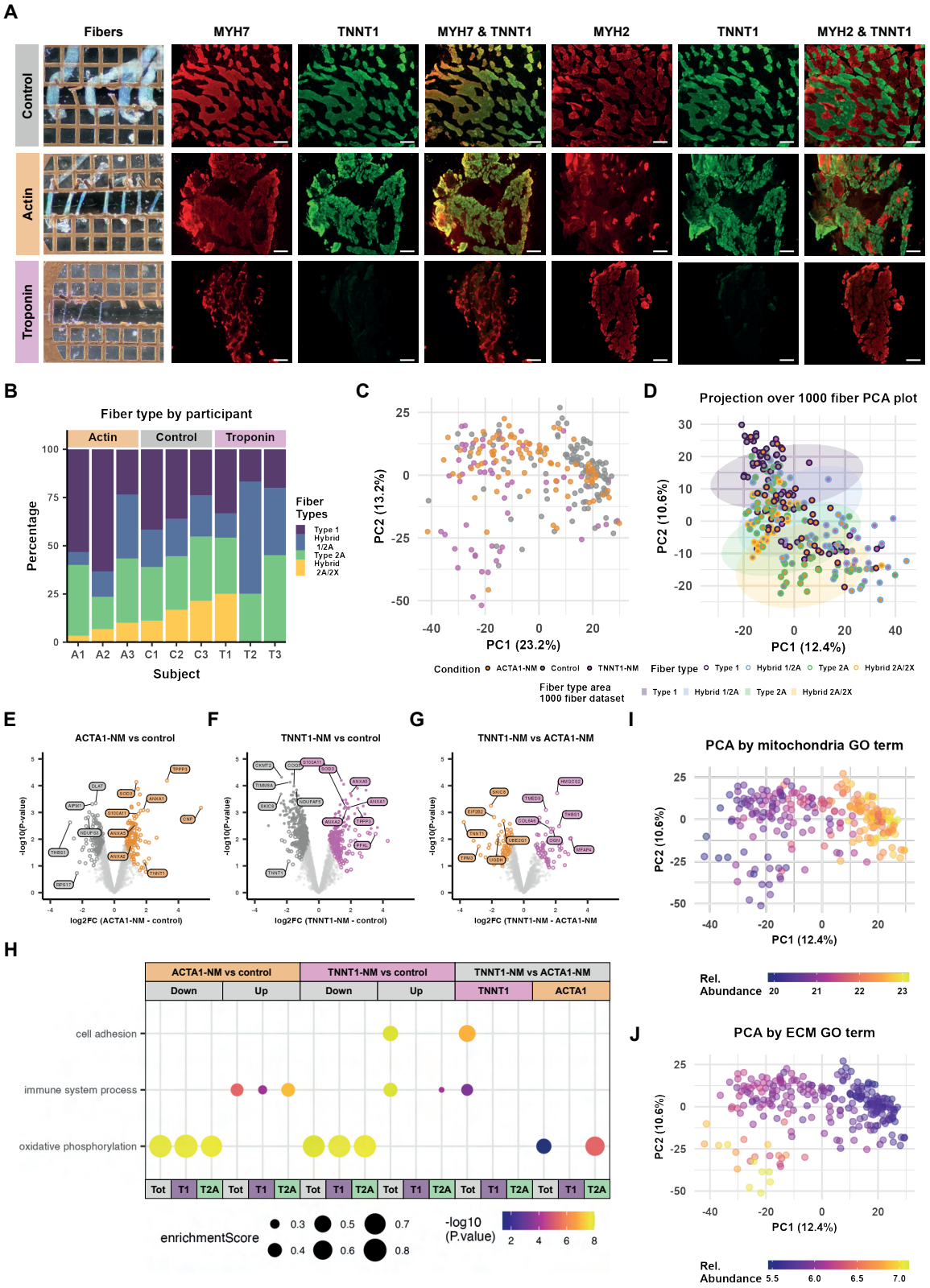

449 **Figure 5. Nemaline myopathies induce a shift towards faster, less oxidative skeletal muscle fibers. (A)**
450 Microscopy images displaying fiber atrophy or hypotrophy and divergent MYH-based fiber type predominance
451 in *ACTA1*- and *TNNT1*-nemaline myopathies (NM). **(B)** MYH-based fiber type proportions by participant. Scaling
452 bar = 100 µm. **(C)** Principal component analysis (PCA) plot of skeletal muscle fibers from nemaline myopathy
453 patients and controls. **(D)** Skeletal muscle fibers from nemaline myopathy patients and controls projected onto
454 PCA plot determined from the 1000 fibers analysed in Fig 2. **(E-G)** Volcano plots comparing the *ACTA1*- and
455 *TNNT1*-nemaline myopathies with control participants and between *ACTA1*- and *TNNT1*-nemaline myopathies.
456 Colored circles represent significantly different proteins at $\pi < 0.05$, darker dots represent significantly different
457 proteins at FDR < 0.05. **(H)** Enrichment analysis of significantly different proteins in the whole proteome and
458 within type 1 and type 2A fibers. **(I-J)** Principal component analysis (PCA) plot colored by extracellular matrix and
459 mitochondria gene ontology (GO) terms.
460
461 We next directly compared each patient group with the samples from healthy controls,
462 resulting in 256 and 552 differentially expressed proteins in *ACTA1*- and *TNNT1*-nemaline
463 myopathies, respectively (**Fig 5E-F & Fig 5 SC, Table S24**). Gene set enrichment analysis
464 identified the coordinated reduction of mitochondrial proteins (**Fig 5H & I, Table S25**).
465 Surprisingly, this was completely independent of MYH-based fiber type (**Fig 5H & Fig 5 S2D-G,**
466 **Table S26**), despite the divergent fiber type predominance between *ACTA1*- and *TNNT1*-
467 nemaline myopathies. Conversely, ribosomal proteins were largely unaffected by nemaline
468 myopathies, although RPS17 was downregulated in *ACTA1* nemaline myopathy (**Fig 5E**).
469
470 Enrichment analysis also identified the up-regulation of immune system process in both
471 *ACTA1*- and *TNNT1*-nemaline myopathies, as well as cell adhesion in *TNNT1*-nemaline
472 myopathy (**Fig 5H**). The enrichment of these extracellular terms, was reflected by extracellular
473 matrix proteins driving the PCA in the negative direction in both PC1 and PC2, i.e. towards the
474 most affected fibers (**Fig 5I**). Both patient groups overexpressed extracellular proteins involved
475 in immune response and the sarcolemma repair machinery, such as annexins (ANXA1, ANXA2,
476 ANXA5)[54,55] and their interactor S100A11[56] (**Fig 5 S2J-K**). This process has been previously
477 reported to be up-regulated in muscle dystrophies[57], yet to our knowledge it has not been
478 associated with nemaline myopathies before. A normal function of this process is required for
479 both sarcolemma membrane repair upon injury and for the fusion of new myoblasts to muscle
480 fibers[55,58]. Therefore, an up-regulation of this process in both patient groups suggests a
481 reparative response to damage caused by myofibril instability.

482

483 The effects of each nemaline myopathy were well correlated (r = 0.736) and displayed
484 reasonable overlap (**Fig 5 S2A & B**), indicating that *ACTA1*- and *TNNT1*-nemaline myopathies
485 induce similar effects on the proteome. Nonetheless, a number of proteins displayed
486 regulation in only *ACTA1*- or *TNNT1*-nemaline myopathies (**Fig 5 S2A & S2C**). MFAP4, a pro-
487 fibrotic protein, was one of the most up-regulated proteins in *TNNT1*-nemaline myopathy
488 whilst unchanged in *ACTA1*-nemaline myopathy. SKIC8, a component of the PAF1C complex,
489 which regulates the transcription of *HOX* genes[59], was down-regulated in *TNNT1*-nemaline
490 myopathy but was unaffected in *ACTA1*-nemaline myopathy (**Fig 5 S2A**). Direct comparisons
491 between *ACTA1*- and *TNNT1*-nemaline myopathies identify a greater effect of *TNNT1*-
492 nemaline myopathies on the reduction of mitochondrial proteins and the increase of immune
493 system proteins (**Fig 5G-H & Fig 5 S2C & S2H-I**). These data are consistent with the greater
494 degree of atrophy/hypotrophy apparent in *TNNT1*- compared to *ACTA1*-nemaline myopathies
495 (**Fig 5A**), indicating that *TNNT1*-nemaline myopathy is the more severe form of the disease.
496

497 These data demonstrate that single muscle fiber proteomics can illuminate clinical biology
498 that is unapparent using targeted approaches such as immunoblotting. Furthermore, these
499 data highlight the limitations of solely relying upon MYH-based fiber typing to describe
500 phenotypic adaptations. Indeed, despite divergent MYH-based fiber type switching in actin
501 and troponin nemaline myopathies, both nemaline myopathies uncouple the MYH-based
502 fiber type from skeletal muscle fiber metabolism, shifting towards a faster, less oxidative
503 muscle proteome.
504

505 **Discussion**

506 Cellular heterogeneity is important to enable tissues to meet a wide range of demands. In
507 skeletal muscle, this has classically been described by fiber types characterized by varying
508 degrees of force production and fatigability. It is apparent, however, that this explains just a
509 fraction of the variation in skeletal muscle fibers, with far greater variability, complexity and
510 nuance residing in skeletal muscle fibers than previously believed. With the advent and
511 development in technologies, these elements that regulate skeletal muscle fibers are now
512 able to be elucidated. Indeed, our data herein, questions the existence of the classical type 2X
513 fiber type as a distinct sub-classification, whilst also identifying determinants of fiber type-

514 independent heterogeneity, which is predominantly regulated post-transcriptionally via
515 ribosomal heterogeneity. By applying our proteomics workflow to samples from nemaline
516 myopathy patients, we further evidence that MYH-based fiber typing does not capture the
517 true heterogeneity of skeletal muscle, particularly when the system is perturbed. Indeed,
518 nemaline myopathies induce a shift towards faster less oxidative fibers regardless of their
519 MYH-based fiber type.
520
521 Skeletal muscle fibers have been classified since the 19th century[1,60]. However, recent omics-
522 based analyses have enabled us to start understanding expression profiles and responses to
523 various stimuli specific to distinct MYH-based fiber types[9-14,22,43,61]. We leveraged
524 complimentary transcriptomics and proteomics workflows, and integrated the results, to
525 explore the transcriptional and post-transcriptional regulation of human skeletal muscle fiber
526 heterogeneity. This pipeline resulted in the observation that the existence of pure type 2X
527 fibers should be questioned, especially at the protein level. Indeed, clustering-based analyses
528 could only confidently identify two distinct clusters, which represented slow and fast skeletal
529 muscle fibers regardless of their exact MYH composition. These findings indicate that we
530 should revert to the view of muscle fiber classification from the early twentieth century and
531 classify human skeletal muscle fibers not into three distinct classifications based on MYHs, but
532 instead into just two clusters based on their metabolic and contractile properties[60].
533
534 Better still, we should consider muscle fiber heterogeneity in multiple dimensions. Over and
535 above the variance within the contractile and metabolic signatures of skeletal muscle, we
536 found that fibers could also be separated by features related to the cell junction and
537 translation machinery. Indeed, we identified ribosomal heterogeneity across skeletal muscle
538 fibers that drives a slow/fast-fiber type independent heterogeneity. Numerous ribosomal
539 proteins displaying variable abundance across fibers regulate selective translation (e.g.
540 RPL10A, RPL38, RPS19 and RPS25)[32-36]. RPL10A is required for efficient nuclear export of the
541 nascent pre-60s complex and therefore ribosomal biogenesis[62]. RPL10A also directly binds
542 internal ribosome entry site (IRES) elements to selectively regulate translation[32,63], whilst
543 depletion of RPL10A in murine embryos is associated with increased translation of mRNAs
544 associated with striated muscle contraction[34]. In RPL38 mutant embryos the translation of
545 *HOX* transcripts is impaired[33], which are involved in cell development, tissue-specific

546 patterning and skeletal muscle plasticity[33,64]. Functionally, RPL10A and RPL38 mutant mice
547 exhibit impaired embryonic development[33,34], demonstrating the physiological relevance of
548 ribosomal heterogeneity.
549
550 The underlying reason for such vast slow/fast-fiber type independent heterogeneity amongst
551 fibers is not immediately obvious, though this could allude to a specialized spatial organization
552 within a muscle fascicle to enable an optimal response to specific forces and loads[65], or
553 specialized cellular or organ communication with other cell types within the muscle
554 microenvironment[66-68]. Indeed, ribosomal heterogeneity (via paralog substitution of RPL3 and
555 RPL3L) has been implicated in skeletal muscle hypertrophy[69]. Multi-omics and spatial
556 applications in concert with functional characteristics of single muscle fibers will further
557 advance our understanding of muscle biology on a multi-omics level[70]. Indeed, as we and
558 others continue to optimize single-cell and single muscle fiber omics-analyses towards ultra-
559 low sample input (as demonstrated here with the analysis of fibers from nemaline myopathy
560 patients), the possibility of combining functional and (multi-)omics approaches in a single
561 muscle fiber is tantalizingly close.
562
563 In analyzing the proteome of single muscle fibers from patients with nemaline myopathies,
564 we also demonstrate the utility, power, and applicability of single muscle fiber proteomics in
565 uncovering clinical pathophysiology in skeletal muscle. In addition to observing expected,
566 albeit divergent, differences in fiber-type proportions in *ACTA1*- and *TNNT1*-nemaline
567 myopathies compared to healthy controls[17], we also identified oxidative and extracellular
568 remodeling, which is uncoupled from this MYH-based fiber type switch. Fibrosis has
569 previously been reported for *TNNT1* nemaline myopathy[17]. However, our analysis builds upon
570 this to also identify the up-regulation of stress-related secreted proteins within the
571 extracellular space, such as annexins, involved in the sarcolemma repair machinery[54-56] in
572 fibers from both *ACTA1*- and *TNNT1*-nemaline myopathy patients. Overall, the up-regulation
573 of annexins in muscle fibers from nemaline myopathy patients may represent a cellular
574 response to rescue severely atrophying fibers.
575
576 Collectively, our data identifies and explains transcriptional and post-transcriptional drivers of
577 heterogeneity within skeletal muscle. In particular, we provide new knowledge of ribosomal

578 heterogeneity in skeletal muscle and how this drives cellular heterogeneity, as well providing
579 data to question long-standing dogmas within skeletal muscle physiology related to the
580 classical definitions of MYH-based fiber-types. In doing so we hope to reignite the debate and
581 ultimately redefine our understanding of skeletal muscle fiber classifications and
582 heterogeneity.
583
584 **Methods**
585 **1000 fiber transcriptomics**
586 **Participant information.** Fourteen participants (12 males / 2 females) volunteered to take part
587 in this study, which was approved by the Ethical Committee of Ghent University Hospital (BC-
588 10237), in agreement with the 2013 Declaration of Helsinki and registered on ClinicalTrials.gov
589 (NCT05131555). General characteristics of the participants can be found in **Table S1**. After oral
590 and written informed consent, participants were medically screened before final inclusion.
591 Participants were young (22-42 years old), healthy (no diseases and non-smoking) and
592 moderately physically active. Maximal oxygen uptake was determined as marker of physical
593 fitness during a graded incremental cycling test, as previously described[71].
594
595 **Muscle biopsy collection.** Muscle biopsies were collected in the rested and fasted state, on
596 three different days, separated by 14 days. As these samples were collected as part of a larger
597 study, on each of these days participants ingested a placebo (lactose), an H1-receptor
598 antagonist (540 mg fexofenadine) or an H2-receptor antagonist (40 mg famotidine) 40
599 minutes before muscle biopsy collection. We have previously shown that these histamine
600 receptor antagonists do not affect the resting skeletal muscle state[71], and no clustering was
601 apparent based on condition in our quality control plots (**Fig 1 S3E & Fig 2 S2B**). Dietary intake
602 was standardized 48 hours before each experimental day (41.4 kcal/kg body weight, 5.1 g/kg
603 body weight carbohydrates, 1.4 g/kg body weight protein and 1.6 g/kg body weight fat per
604 day), followed by a standardized breakfast on the morning of the experimental day (1.5 g/kg
605 bodyweight carbohydrates). Muscle biopsies of the *m. vastus lateralis* were then collected
606 after local anaesthesia (0.5 mL of 1% Xylocaïne without epinephrine) using the percutaneous
607 Bergström technique with suction[72]. The muscle samples were immediately submerged in
608 RNA*later* and stored at 4 °C until manual fiber dissection (max. 3 days).
609

610 **Single fiber isolation.** Freshly excised muscle fiber bundles were transferred to fresh RNA*later*
611 in a petri dish. Individual muscle fibers were then manually dissected using a
612 stereomicroscope and fine forceps. Twenty-five fibers were dissected per biopsy, with special
613 care to select fibers from different sections of the biopsy. After dissection, each fiber was
614 carefully submerged in 3 µL of lysis buffer (SingleShot Cell Lysis kit, Bio-rad), containing
615 proteinase K and DNase enzymes to remove unwanted proteins and DNA. Next, cell lysis and
616 protein/DNA removal was initiated by short vortexing, spinning liquid down in a
617 microcentrifuge and incubation at room temperature (10 min). Lysates were then incubated
618 for 5 min at 37 °C and 5 min at 75 °C in a thermocycler (T100, Bio-Rad), immediately followed
619 by storage at -80 °C until further processing.
620
621 **Sequencing library preparation.** Illumina-compatible libraries from polyadenylated RNA were
622 prepared from 2 µL of the muscle fiber lysates using the QuantSeq-Pool 3' mRNA-Seq library
623 prep kit (Lexogen). Detailed methodology can be found in the manufacturer guidelines. The
624 process was initiated by reverse transcription for first strand cDNA synthesis, during which
625 Unique Molecular Identifiers (UMIs) and sample-specific i1 barcodes were introduced
626 enabling sample pooling and reducing technical variability in the downstream process. Next,
627 cDNA from 96 fibers was pooled and purified using magnetic beads, followed by RNA removal
628 and second strand synthesis by random priming. Libraries were purified using magnetic beads,
629 followed by addition of pool-specific i5/i7 indices and PCR amplification. A last purification
630 step was performed, finalizing the Illumina-compatible libraries. A high sensitivity small DNA
631 Fragment Analysis kit (Agilent Technologies, DNF-477-0500) was used to assess the quality of
632 each library pool.
633
634 **Illumina sequencing.** The individual pools were further equimolarly (2 nM) pooled, based on
635 Qubit-quantified concentrations. The final pool was subsequently sequenced with a NovaSeq
636 S2 kit (1 x 100 nucleotides) with a loading of 2 nM (4% PhiX) in standard mode on a NovaSeq
637 6000 instrument.
638
639 **Primary data processing.** Our pipeline was based on the QuantSeq Pool data analysis pipeline
640 from Lexogen (https://github.com/Lexogen-Tools/quantseqpool_analysis). First, the data was
641 demultiplexed based on the i7/i5 indices with bcl2fastq2 (v2.20.0). The next demultiplexing

642 step was performed via idemux (v0.1.6) according to the i1 sample-specific barcodes in read
643 2, followed by extraction of UMI sequences with umi_tools (v1.0.1). Trimming of the reads
644 was then performed in multiple rounds with cutadapt (v3.4), with removal of too short reads
645 (length < 20) or reads consisting entirely of adapter sequences. Reads were then aligned to
646 the human genome with STAR (v2.6.0c), followed by BAM file indexing with SAMtools (v1.11).
647 Duplicates of reads were removed with umi_tools (v1.0.1). Finally, counting of the alignments
648 was performed with featureCounts from Subread (v2.0.3). At several intermediate steps
649 during the pipeline, quality control with performed with FastQC (v0.11.9).
650
651 **Initial Seurat processing.** All further bioinformatics processing and visualization was
652 performed in R (v4.2.3), primarily with the Seurat v4 workflow[73]. The individual UMI counts
653 and metadata matrices were thus transformed into a Seurat object. Genes with expression in
654 less than 30% of all fibers were removed. Low-quality samples were then removed based on
655 a minimum threshold of 1000 UMI counts and 1000 detected genes. This resulted in a total of
656 925 fibers that passed all quality control filtering steps. Normalization of UMI counts was
657 performed using the SCTransform v2 Seurat method[74], including all 7418 detected features
658 and regressing out participant variation. All relevant metadata can be found in **Table S27**.
659
660 **Proteomics**
661 **Sample collection - 1000 fiber proteome**
662 **Participant information**. Stored biobank muscle specimens were used for the purpose of the
663 present study (Clinicaltrials.gov identifier: NCT04048993). The specimens were collected from
664 five active and healthy male volunteers (aged 21-35 years) who gave their written and oral
665 informed consent with approval from the Science Ethics Committee of the Capital Region in
666 Denmark (H-1-2012-090) and complied with the guidelines of the 2013 Declaration of
667 Helsinki. General characteristics of the participants can be found in **Table S1.** Participants were
668 young, healthy (no diseases and non-smoking) and moderately physically active.
669
670 **Muscle biopsy collection.** Participants arrived in the morning after an overnight fast and
671 rested in the supine position for 1 hour. Then, local anesthesia (2-3 mL Xylocaine 2%; lidocaine
672 without epinephrine, AstraZeneca, Denmark) was applied under the skin above the fascia at
673 the belly of the *m. vastus lateralis* muscle. A muscle biopsy was sampled through a small 3-4

674 mm incision using a Bergström needle with suction. The muscle biopsy specimen was snap-
675 frozen in liquid nitrogen and stored at −80°C until analysis.
676
677 **Single muscle fiber isolation.** Muscle fibers were isolated from freeze-dried specimens as
678 previously described[22]. In brief, muscle biopsies were freeze-dried for 48 hours. Subsequently,
679 fibers were isolated in a humidity- and temperature-controlled room (humidity of 25%) using
680 fine forceps under a stereomicroscope. Approximately 200 single muscle fibers were isolated
681 for each biopsy, resulting in a total of 1038. To ensure the fibers settled at the bottom of the
682 tube, each fiber-containing tube underwent centrifugation at 20,000 g using a small
683 centrifuge. Next, fibers were resuspended in 15 µL of lysis buffer (1% sodium dodecyl sulfate
684 (SDC), 40 mM chloroacetamide (CAA), 10 mM dithiothreitol (DTT) in 50 mM Tris pH 8.5).
685
686 **Sample collection – myopathy**
687 **Participant information.** Six patients with severe nemaline myopathy were selected from our
688 nemaline myopathy study cohort. Three patients had pathogenic variants in *ACTA1*,
689 representing the conventional severe form, and three patients had pathogenic variants in
690 *TNNT1*, resulting in a rare, progressive form of nemaline myopathy. Three healthy individuals
691 with no history of neuromuscular disease were used as controls (**Table S20**).
692
693 **Muscle biopsy collection.** Healthy control participant biopsies (n = 3) were used from an
694 original study[75], and were therefore collected, snap frozen in liquid nitrogen and stored in -
695 80℃ as per that originally described. For the present study, a fragment of this stored biopsy
696 was dissected under sterile, frozen conditions before being prepared for single myofiber
697 isolation (detailed below). Acquisition of biopsies of healthy control patients was approved by
698 local ethics committee (Copenhagen and Frederiksberg) in Denmark (hs:h-15002266). Those
699 of myopathy patients were consented, stored, and used in accordance with the Human Tissue
700 Act under local ethical approval in United Kingdom (REC 13/NE/0373). All procedures were
701 carried out in accordance to the Declaration of Helsinki.
702
703 **Single fiber isolation.** Dissected fragments of muscle biopsy were placed in ice-cold, 22 micron
704 filtered relaxing solution (4 mM Mg-ATP, 1 mM free Mg^{2+}, $10^{-6.00}$ mM free Ca^{2+}, 20 mM
705 imidazole, 7 mM EGTA, 14.5 mM creatine phosphate, KCl to an iconic strength of 180 mM and

706 pH to 7.0)[76] for ~3 minutes before being immersed in fresh relaxing solution on a sterile petri
707 dish and mounted on ice under a dissection microscope for single fiber isolation. Fibers were
708 cleaved from the tissue/biopsy ensuring a variety of sample/biopsy locations were used and
709 that only single fibers were selected. Following isolation, fibers were manually moved to a
710 sterile 96-well plate containing 15 µL of lysis buffer (identical to that detailed above) where
711 the tweezers containing the fiber were submerged, spun and agitated in lysis buffer to ensure
712 the fibers dissociated from the tweezers. To ensure fibers were settled to the bottom of the
713 well, the 96-well plate was subjected to gentle vortexing and centrifugation (1,000 g).
714
715 **Proteomics analysis**
716 **Sample preparation.** Samples from both proteomics studies followed the same sample
717 preparation workflow. In order to extract the proteins, samples were boiled at 95°C in a
718 thermomixer with gentle shaking (800 rpm) and sonicated in a bioruptor instrument with 30
719 seconds on/off cycles for 15 minutes. A small 5 µL fraction of lysate from each sample was
720 saved for antibody-based fiber typing of the 1000 fiber samples. Next, samples were
721 processed following a modified version of the in-solution digestion sample preparation
722 protocol. In brief, total volume was adjusted to 50 µl by addition of digestion buffer, containing
723 50 mM Tris PH 8.5 buffer, an enzyme to protein ratio of 1:500 LysC (Wako) and a 1:100 enzyme
724 to protein ratio of trypsin (Promega). SMF lysates were digested overnight in a thermomixer
725 set to 37° C and 800 rpm. The next day, protein digestion was quenched by addition of 50 µl
726 of 2% trifluoroacetic acid (TFA) in isopropanol. Peptides were desalted using in-house
727 prepared single-use reverse-phase StageTips containing styrenedivinylbenzene reverse-phase
728 sulfonate (SDB-RPS) disks. Then, desalted peptides were loaded in Evotips (Evosep) following
729 manufacturer instructions prior LC-MS/MS analysis.
730
731 **Proteomics library preparation.** Fibers from the five healthy control individuals participating
732 in the 1000 fiber study were carefully dissected and combined in order to create a pooled
733 fiber lysate. Then, 200 µg of protein corresponding to each participant-specific lysate were
734 pooled together into one final protein lysate that was processed following the same sample
735 preparation workflow just described. 20 µg of desalted peptides were fractionated using High
736 pH Reverse-Phase Chromatography (HpH-RP). Fractionation was carried out on a Kinetex 2.6
737 µm EVO C18 100 Å, 150 x 0.3 mm column manufactured by Phenomenex and using an EASY-

738 nLC 1200 System (Thermo) operating at 1.5 µL/min. Separation was accomplished using a 62
739 min step-gradient starting from 3% to 60% solvent B (which consisted of 10 mM TEAB in 80%
740 acetonitrile) and solvent A (containing 10 mM TEAB in water). The total run time was 98 min,
741 which included wash and column equilibration. Throughout the fractionation, peptides were
742 eluted and collected every 60 s, obtaining 96 single fractions without concatenation. Finally.
743 200 ng of HpH-RP fractionated peptides were loaded, concentrated and desalted on Evotips
744 (Evosep) following the instructions provided by the manufacturer.
745
746 **Liquid chromatography tandem mass spectrometry**. Proteomics measurements were
747 performed using LC-MS instrumentation consisting of an Evosep One HPLC system (Evosep)[20]
748 coupled via electrospray ionization to a timsTOF SCP mass spectrometer (Bruker). Peptides
749 were separated utilizing 8 cm, 150 µM ID columns packed with C18 beads (1.5 µm) (Evosep).
750 Chromatographic separation was achieved by the '60 samples per day' method, followed by
751 electrospray ionization through a CaptiveSpray ion source and a 10 µm emitter into the MS
752 instrument. Single muscle fiber peptides were measured in DIA-PASEF mode following a
753 previously described method[21], while library fractions were measured using DDA-PASEF. In
754 brief, the DDA-PASEF scan range encompassed 100 - 1700 m/z for both MS and MS/MS, and
755 TIMS mobility range was set to 0.6 – 1.6 (V cm^{-2}). Both TIMS ramp and accumulation times
756 were configured to 100 ms, and 10 PASEF ramps were recorded for a total cycle time of 1.17
757 s. The MS/MS target intensity and intensity threshold were defined as 20.000 and 1.000,
758 respectively. An exclusion list of 0.4 min for precursors within 0.015 m/z and 0.015 V cm^{-2}
759 width was also activated. For DIA-PASEF the scan range was established at 400-1000 (m/z),
760 the TIMS mobility range to 0.64-1.37 (V cm^{-2}), and ramp and accumulation times were both
761 set to 100 ms. A short-gradient method was used, which included 8 DIA-PASEF scans with
762 three 25 Da windows per ramp, resulting in an estimated cycle time of 0.95 sec.
763
764 **MS data processing**. Library files were processed using the MS-Fragger functionality within
765 Fragpipe v19.0 under the SpecLib workflow with default settings, including a minimum
766 peptide length of seven amino acids and maximum of two missed cleavages allowed[77]. Spectra
767 were searched against a human reviewed FASTA from Uniprot (March 2022, 20410 entries)
768 and the output library contained a total of 5350 protein groups and 84383 precursors. Sample
769 raw MS files were analyzed using DIA-NN version 1.8[78] in a library-based manner against the

770 MS library just described. Protein groups quantification was based on proteotypic peptides,
771 neural network was set to double-pass mode, quantification strategy was set to "Robust LC
772 (high accuracy)" and the match between runs options was enabled, the rest of parameters
773 remained as default, which included precursor FDR set to 1% and peptide length of 7-30 amino
774 acids.
775
776 **Data processing**. Further data analysis was performed under the R environment (R version
777 4.22). Both a metadata data frame containing sample and participant information and the
778 "PG_matrix.tsv" file from DIA-NN's output were loaded in RStudio. The 1000 fiber data frame
779 was filtered to remove samples with less than 50% valid protein intensity values, resulting in
780 a total of 974 fibers. Next, rows were filtered to remove proteins with less than 30% valid
781 values across samples, resulting in a total of 1685 proteins. Regarding the myopathy dataset,
782 after filtering samples for 50% valid values, the number of samples was 250. We included in
783 the analysis proteins that were quantified in 70% of the samples in at least one condition
784 (conditions: control, actin myopathy and troponin myopathy), resulting in a total of 1545
785 proteins. Both data frames were then log2 transformed and normalized using the
786 *normalizeBetweenArrays()* function from the limma package, with the method argument set
787 to quantile[79]. Then, batch correction through the *ComBat()* function from the sva package[80]
788 was applied to minimize the effect of the three technical batches originated during mass
789 spectrometry measurement. Finally, missing values were replaced by random numbers from
790 a Gaussian distribution with the default settings of the *tImpute()* function from the PhosR
791 package[81]. All relevant metadata for the 1000 fiber proteome and nemaline myopathy
792 datasets can be found in **Tables S28 and S29, respectively**.
793
794 **Bioinformatics analysis**
795 **Transcriptome and proteome dynamic range.** The expression/intensity for each gene/protein
796 was calculated relative to the total counts/intensity for each fiber. This value was then
797 averaged across fibers in each dataset and log10-transformed. The overlap of detected
798 features between both datasets were analyzed using the *VennDiagram* package (v 1.7.3).
799
800 **Coefficient of variation – proteomics.** For each of the 96 well plates used during the MS
801 measurement of the 1000 fiber study, one technical control sample was included in A1

802 position to monitor total ion current intensity and quality control of the runs (a total of eleven
803 technical controls). The coefficient of variation between proteins was calculated by dividing
804 the standard deviation by the mean of the LFQ intensities from each protein across technical
805 replicates and then multiplied by one hundred.
806
807 **Correlation analyses.** Mean log2 transformed transcript counts, protein intensities, and/or
808 fold change values across fibers were calculated, filtered for shared proteins/genes and
809 Pearson correlation was calculated.
810
811 **Omics-based fiber typing.** Normalized counts and raw LFQ intensities were retrieved from
812 well-described contractile proteins that have a slow (MYH7, TNNT1, TPM3, ATP2A2 and MYL3)
813 and fast (MYH2, MYH1, TNNT3, TPM1, ATP2A1 and MYL1) isoform[1]. For each isoform
814 combination, the relative expression of each was then calculated and samples were ordered
815 from high to low. The mathematical bottom knee for each curve was then determined using
816 the *barcodeRanks()* function in the DropletUtils package (v 1.18.1). This threshold was used
817 to assign fiber types as pure (type 1, type 2A or type 2X) or hybrid (hybrid 1/2A, hybrid 2A/2X
818 or hybrid 1/2X) (**Table S6**). For the features with only two isoforms, fibers were assigned as
819 'slow', 'fast' or 'hybrid'. To determine the overlap of the contractile features assigning a fiber
820 as being slow, upset plots were generated using the *upset()* function of the ComplexUpset
821 package (v 1.3.3), and then simplified to bar plots.
822
823 **Principal Component Analysis (PCA).** PCA was performed using the *RunPCA()* function of the
824 Seurat package. Scree plots were based on the *fviz_eig()* function of the factoextra package (v
825 1.0.7), which worked after PCA with *prcomp()*.
826
827 **Seurat clustering.** Uniform Manifold Approximation and Projection (UMAP) clustering was
828 performed based on the K-nearest neighbor graph with the first 6 dimensions as input for
829 both the transcriptome and proteome datasets (**Fig 1 S3D-E**). Feature plots were generated
830 using the *FeaturePlot()* function. UMAP plots were colored based on different criteria (MYH-
831 based fiber types, participant, test day) stored in the metadata.
832

833 **Enrichment analysis.** Genes and protein sets were processed to obtain lists of features that
834 were differentially expressed or, in the case of the top PCA drivers, in the top 5% drivers for
835 the positive and negative direction of the first and second principal component. Over-
836 representation analysis was then performed on these features with the *enrichGO()* and
837 *simplify()* function of the clusterProfiler package (v 4.6.2)[82] using all gene ontology terms.
838 Obtained lists of significant terms were manually curated to extract interesting and relevant
839 terms.
840
841 **Hierarchical clustering of ribosomal proteins.** Raw proteomics data was log2 transformed and
842 filtered to contain proteins enlisted in the 'cytosolic ribosome' GO term, followed by Z-scoring
843 prior heatmap visualization using the *pheatmap()* function from the Pheatmap package (v
844 1.0.12). The number of clusters was determined by visual inspection and assigning a value of
845 3 to the *cuttree*() function.
846
847 **Differential expression analysis**. To avoid artificially inflated p-values, which would arise from
848 regarding every fiber as an independent replicate, we employed a pseudobulk differential
849 expression analysis approach. We mathematically downsampled the total data points to one
850 value per MYH-based fiber type per participant by aggregating (transcriptomics) or taking the
851 median value (proteomics). Transcriptomics data were further processed using the DESeq2
852 pipeline (v 1.38.3)[83] with a '~ participant + fiber type' statistical model. 1000 fiber proteomics
853 data was processed using the limma (v 3.54.2) workflow, fitting the data to a linear model
854 defined as: '~ 0 + fiber type + participant', whereas the myopathy dataset was fitted to '~ 0 +
855 condition' for the comparisons between conditions and '~ 0 + fiber type and condition' for the
856 comparisons including fiber type. Fitted models were then subjected to gene ranking using an
857 empirical Bayes method using *eBayes*() prior extracting the results through *topTable*(), with p-
858 value adjustment set to Benjamini-Hochberg, both functions from the limma package.
859 Threshold for significantly different genes/proteins was defined as adjusted p-values smaller
860 than 0.05. For the nemaline myopathy dataset, the Xiao significance score was applied, which
861 combines expression fold change and statistical significance[84]. Proteins with a Xiao score
862 under 0.05 were regarded as differentially expressed between conditions.
863

Transcription factor motif enrichment. This analysis was performed using the gProfiler webtool (https://biit.cs.ut.ee/gprofiler/gost), with the list of differentially expressed genes in each slow/fast fiber type as input, ordered based on adjusted p-values (transcriptomics data). Data was sourced from the TRANSFAC database.

Non-coding RNA. For the transcriptomics data, the biotype of each gene was determined using the 'GENEBIOTYPE' column using the AnnotationDbi package (v 1.60.2) with the EnsDb.Hsapiens.v86 database. Genomic location interrogation was performed using the UCSC Human Genome Browser (https://genome.ucsc.edu). Tissue-specific gene expression of interesting long non-coding RNAs was explored using the GTEx Portal database.

Microprotein identification.

Construction of putative lncRNA-encoded protein database

RNA sequences of the non-coding transcripts were extracted using the *getSequence() function from the biomaRt package* (v 2.56.1)*,* with 'transcript_exon_intron' as the *seqType.* Both intergenic (lincRNA) and antisense long non-coding RNA (lncRNA) transcripts were utilized for database construction. A six-frame-translation was used to translate the corresponding RNA sequences into the proteins, as well as ORFfinder NCBI functionality (https://www.ncbi.nlm.nih.gov/orffinder/) was used to extract open reading frames (ORFs) from the transcripts. Minimal ORF length was set to 75 nucleotides, genetic code was set to "Standard" and "Any sense codon" was used, as a start codon, to extract maximum number of open reading frames. The obtained protein fasta file contained multiple entries for each gene name, ensured by various combinations of: i) transcript identifiers, ii) ORF identifiers and iii) start:stop codons.

Identification of lncRNA-encoded proteins

DIA raw MS data were analysed with Spectronaut v18 using an in-house generated sample-specific fasta, comprised of the reviewed human proteome (proteome ID: UP000005640, 20 426 proteins, downloaded Sep 2023) and lncRNA-encoded protein sequences (125 223 proteins), in directDIA mode. The default settings were used unless otherwise noted. Data filtering was set to "Qvalue". False discovery rate (FDR) was set to 1% at peptide precursor level and 1% at protein level. Top3 peptide precursors were used for protein

896 quantification. The downstream data analysis was performed using in-house developed R
897 script.
898
899
900 **PCA projection**. The 1000 fiber and myopathy data sets were initially filtered to remove non-
901 overlapping proteins. Then, they were combined and normalized using the
902 *normalizeBetweenArrays()* function from the limma package. The normalization method used
903 was "quantile" to ensure that both data sets had the same distributions and were comparable.
904 Subsequently, the merged data set was divided back into the two separate data sets, namely
905 the 1000 fiber data set and the myopathy data set. For the 1000 fiber data set, PCA was
906 calculated using the *prcomp()* function. Moving on, the myopathy data set was multiplied by
907 the PC loadings obtained from the 1000 fiber dataset to generate its PCA projection. Finally,
908 the PCA projections from the myopathy samples were plotted on the top of the 1000 fiber
909 PCA visualization.
910
911 **Muscle-specific ribosomal gene signature**
912 The skeletal muscle-specific ribosomal gene signature, consisting of log2 fold change values
913 comparing the mRNA expression of ribosomal subunits in skeletal muscle compared to 52
914 other human tissues, was downloaded from Panda et al[85]. Log2 fold change values were
915 ranked to identify ribosomal proteins with the highest overexpression in human skeletal
916 muscle.
917
918 **Structural Analysis of Ribosomal Proteins**
919 The human 80S ribosome structural model (Protein Data Bank: 4V6X) was downloaded from
920 the Protein Data Bank website (RCSB PDB). Visualization and editing of the ribosomal
921 structure, and preparation of figures and movies were performed in UCSF ChimeraX[86].
922
923 **Antibody-based fiber typing**
924 Dot blot was conducted following a previously described protocol with a few modifications[22].
925 Initially, two identical PVDF membranes were activated using 96% ethanol and washed with
926 transfer buffer. Subsequently, the membranes were placed on wet filter paper with transfer
927 buffer until they dried. Next, 1 µL of fiber lysate was spotted at the same position on both

928 membranes, and the membranes were allowed to dry. Reactivation of the membranes was
929 carried out using 96% ethanol, followed by gentle washing with TBST. The membranes were
930 then blocked in TBST containing 5% skim milk for 15 minutes. After blocking, the membranes
931 were washed three times with TBST and incubated with the primary antibody solution of
932 either anti-MYH7 (A4.840) or anti-MYH2 (A4.74), both from Developmental Studies
933 Hybridoma Bank (DSHB) at a dilution of 1:200 in TBST containing 1% skim milk for one hour.
934 Subsequently, the membranes were gently washed three times with TBST and incubated with
935 the secondary antibody (anti-mouse) at a dilution of 1:20,000 in TBST containing 1% skim milk
936 for two hours. Finally, the membranes were washed three times for five minutes each with
937 TBST and visualized using Immobilon Forte (Milipore) in a ChemiDoc XRS+ (Bio-Rad) imaging
938 system.
939
940 **RNAscope**.
941 8µm sections from fixed-frozen human muscle biopsies were used for RNAscope labelling and
942 subsequent immunohistochemistry (IHC). For detection of RP11-255P5.3 and LINC01405
943 commercially available RNAscope Multiplex Fluorescent Assay V2 (Advanced Cell Diagnostics)
944 and probes against Lnc-ERCC5-5-C1 (# 1276851-C1), and LINC01405-C2 (# 549201-C2)
945 (Advanced Cell Diagnostics), were used according to the manufacturer's protocols. To control
946 tissue quality Positive 3-plex probe (# 320881) and negative 3-plex probe (# 320871) were
947 used. To visualize different subtypes of muscle fibers, sections after RNAscope were blocked
948 with 5% donkey serum and incubated with antibodies against MYH2 (A4.74-s (1:5); DSHB) and
949 MYH7 (A4.840 (1:5); BSHD) overnight. After washing sections were incubated with Alexa Flour
950 488-conjugated Donkey Anti-Mouse IgG, Fcγ Subclass 1 and DyLightTM405-conjugated
951 Donkey Anti-Mouse IgM secondary antibodies respectively and mounted with ProLong™
952 Diamond Antifade Mountant (Invitrogen). Slides were imaged using Zeizz Axio Observer
953 microscope equipped with Axiocam 702 camera.
954
955 **Immunostaining for muscle sections**
956 Immunolabelling was performed on 10 µm cryosections, fixed in 4% PFA (10 min),
957 permeabilized in 0.1% Triton X-100 (20 min) and blocked in 10% Normal Goat Serum (50062Z,
958 Life Technologies) with 0.1% BSA (1 h). Sections were incubated o/n (4ºC) with primary
959 antibodies against MYH7 (mouse monoclonal A4.951, Santa Cruz, sc-53090, diluted 1:25) or

MYH2 (mouse monoclonal SC71, DSHB, 1:25), each combined with primary antibody against TNNT1 (rabbit polyclonal HPA058448, Sigma, diluted 1:500) in 5% goat serum with 0.1% BSA and 0.1% Triton X-100. Alexa Fluor Goat anti-Mouse 647 (A21237) was used as the secondary antibody for the MYHs and Alexa Fluor Donkey anti-Rabbit 488 (A11034) for the tropomyosin (Life Technologies, 1:500 each in 10% Normal Goat Serum). Fluorescent images were obtained with a 10x objective on a Zeiss Axio Observer 3 fluorescence microscope with a Colibri 5 led detector, combined with Zeiss Axiocam 705 mono camera, using Zen software (Zeiss). For visualization purposes, a selection of fibres were mounted on copper grids glued on a microscopy slide, and imaged under a stereomicroscope.

Acknowledgments

Mass spectrometry analyses were performed by the Proteomics Research Infrastructure (PRI) at the University of Copenhagen (UCPH), supported by the Novo Nordisk Foundation (NNF) (grant agreement number NNF19SA0059305). This work was generously funded by grants from the Novo Nordisk Foundation (NNF-0070539; to JO), the Foundation Building Strength For Nemaline Myopathy (to JO) and the Research Foundation Flanders (G080321N, 11B4220N and 1268023N; to WD, TVdS and EL, respectively). Several plots (Fig 1A, Fig 1S1A, Fig 5S2H) were made with BioRender.com. The authors would like to thank Leonidas Lundell & Lars Roed Ingerslev for their input on data analysis and visualization.

Author contributions

Conceptualization: RMJ, TVdS, BS, EL, PM, JV, JO, MH, WD, ASD

Methodology: RMJ, TVdS, BS, JL, RAS, DS, OD, AVdL, EL, LMA, KVV, MW, PM, JV, MH, WD, ASD

Software: RMJ, TVdS, BS, DS, LMA, JA

Validation: RMJ, TVdS, BS, JL, PM, JV, WD, ASD

Formal Analysis: RMJ, TVdS, BS, JL, DS, LMA

Investigation: RMJ, TVdS, BS, JL, RAS, DS, AVdL, EL, LMA, KVV, NY, AW, RVT, RES, EZ, MWL

Resources: RES, EZ, MWL, MW, PM, JV, JO, MH, WD, ASD

Data curation: RMJ, TVdS, BS, JL, DS, LMA, JA

Writing – Original Draft: RMJ, TVdS, BS, WD, ASD

Writing – Review and Editing: RMJ, TVdS, BS, JL, RAS, DS, OD, AVdL, EL, LMA, KVV, NY, JA, AW, RVT, RES, EZ, MWL, MW, PM, JV, JO, MH, WD, ASD

Visualization: RMJ, TVdS, BS, JL, LMA, OD

Supervision: BS, PM, JV, JO, MH, WD, ASD

Project Administration: RMJ, TVdS, BS, WD, ASD

Funding Acquisition: TVdS, EL, PM, JV, JO, MH, WD, ASD

Supplemental Figures

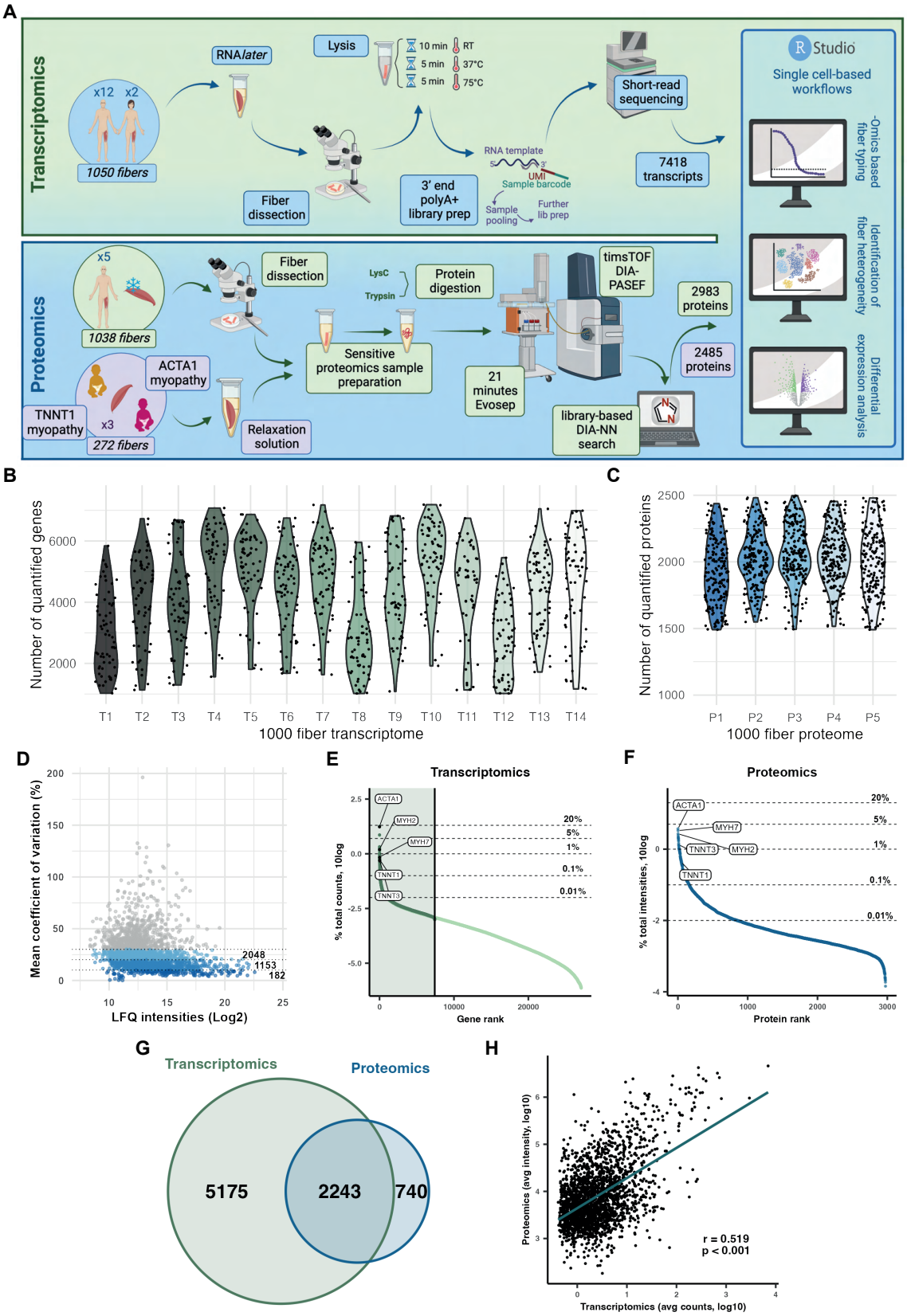

Figure 1 S1. Quality control of novel transcriptomic and proteomic workflows. (**A**) Detailed schematic of developed workflows. (**B-C**) Number of quantified genes/proteins by participant and sample in 1000 fiber transcriptomics and proteomics. (**D**) Coefficient of variation by protein in 1000 fiber proteomics. (**E-F**) Dynamic

range of genes in 1000 fiber transcriptomics and of proteins in 1000 fiber proteomics. (**G**) Overlapping features within 1000 fiber transcriptomics and proteomics. (**H**) Correlation between features within 1000 fiber transcriptomics and proteomics.

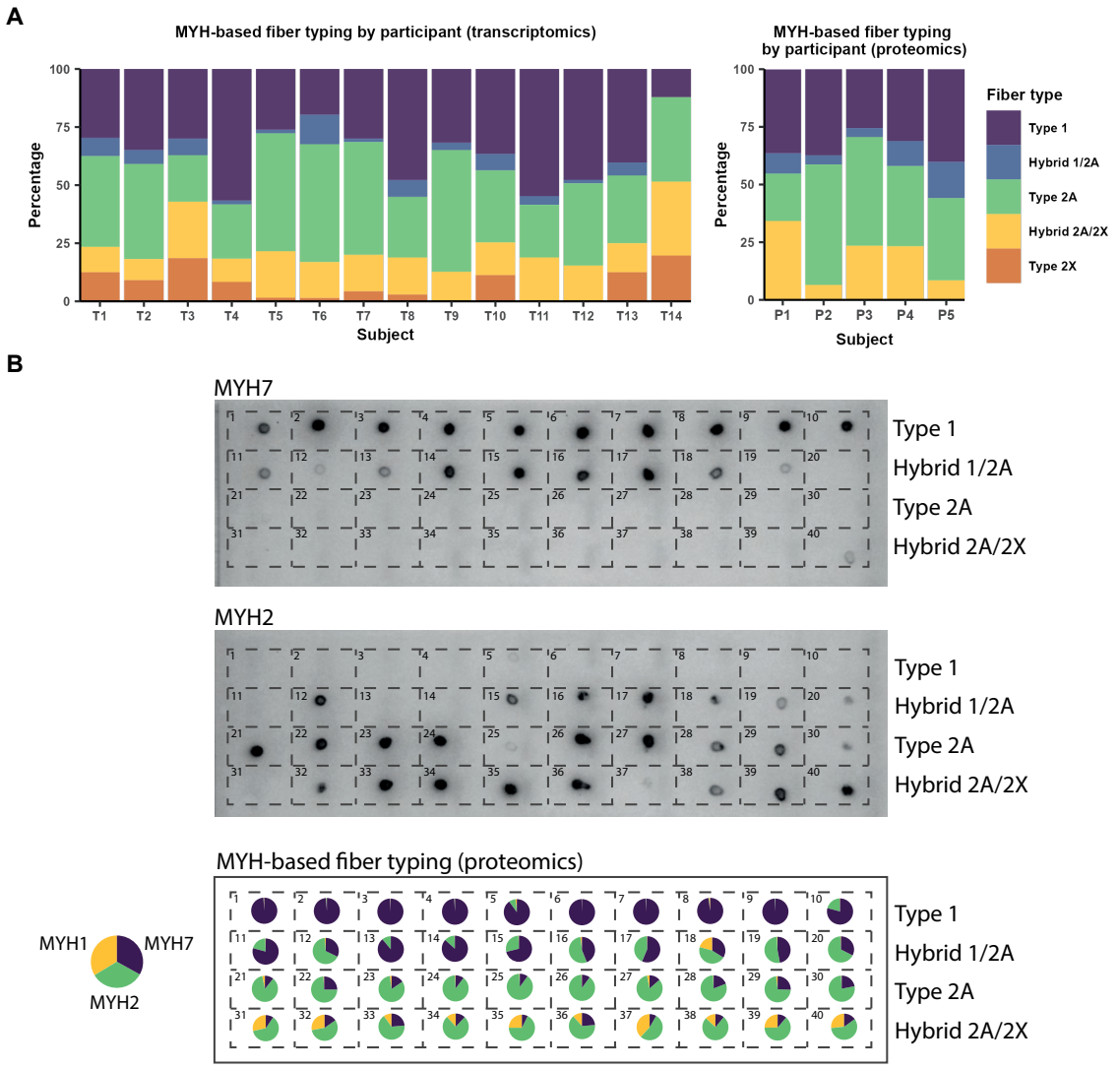

Figure 1 S2. Higher sensitivity with proteomics compared to standard dot blotting. (**A**) MYH-based fiber type proportions by participant. (**B**) Comparison between dot blot- and proteomics-based fiber typing.

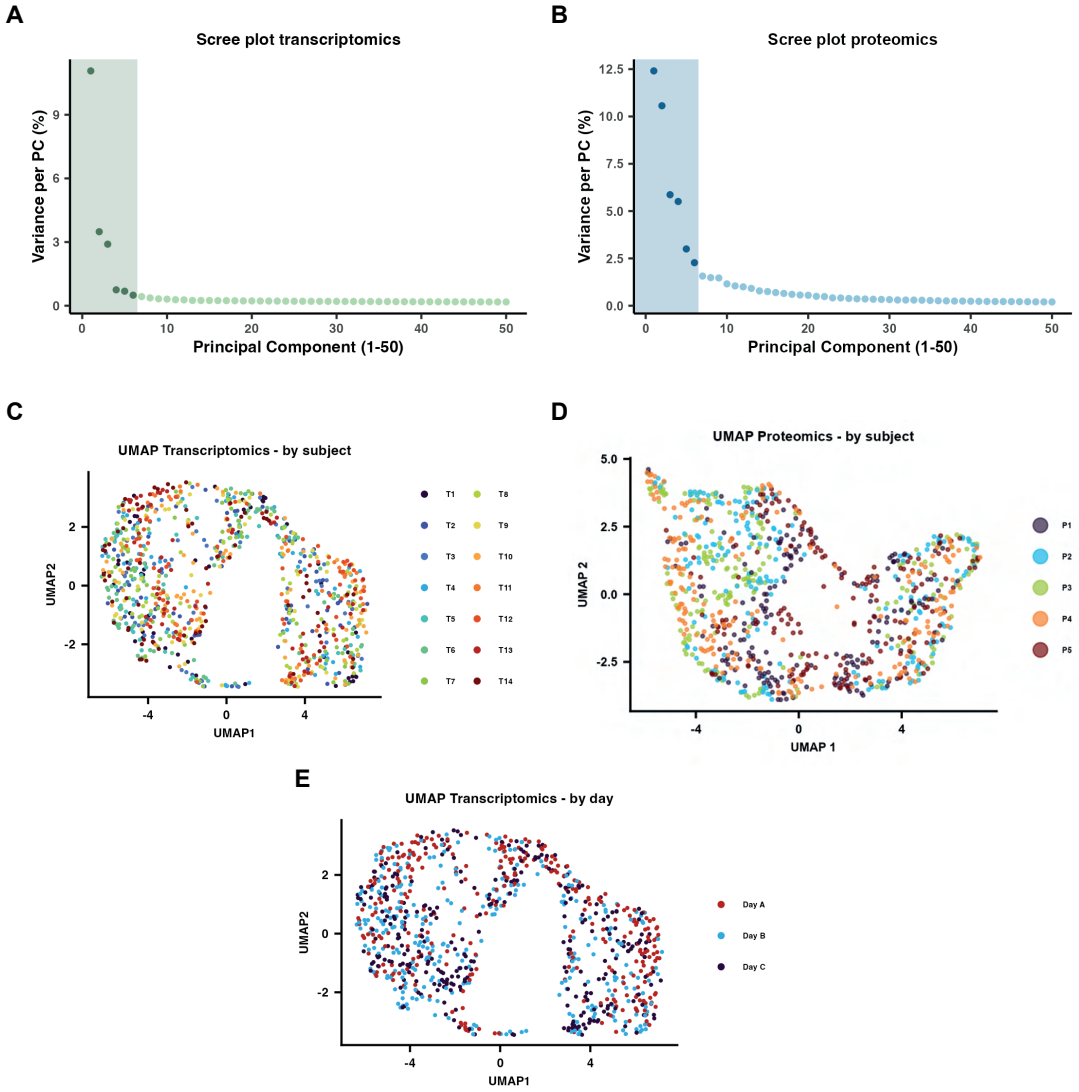

Figure 1 S3. Clustering of transcriptomic and proteomic data. (**A-B**) Scree plots of transcriptomics and proteomics. Colored box indicates the number of principal components used for clustering. (**C-D**) 1000 fiber transcriptomics and proteomics UMAP colored by participant. (**E**) 1000 fiber transcriptomics UMAP colored by trial day.

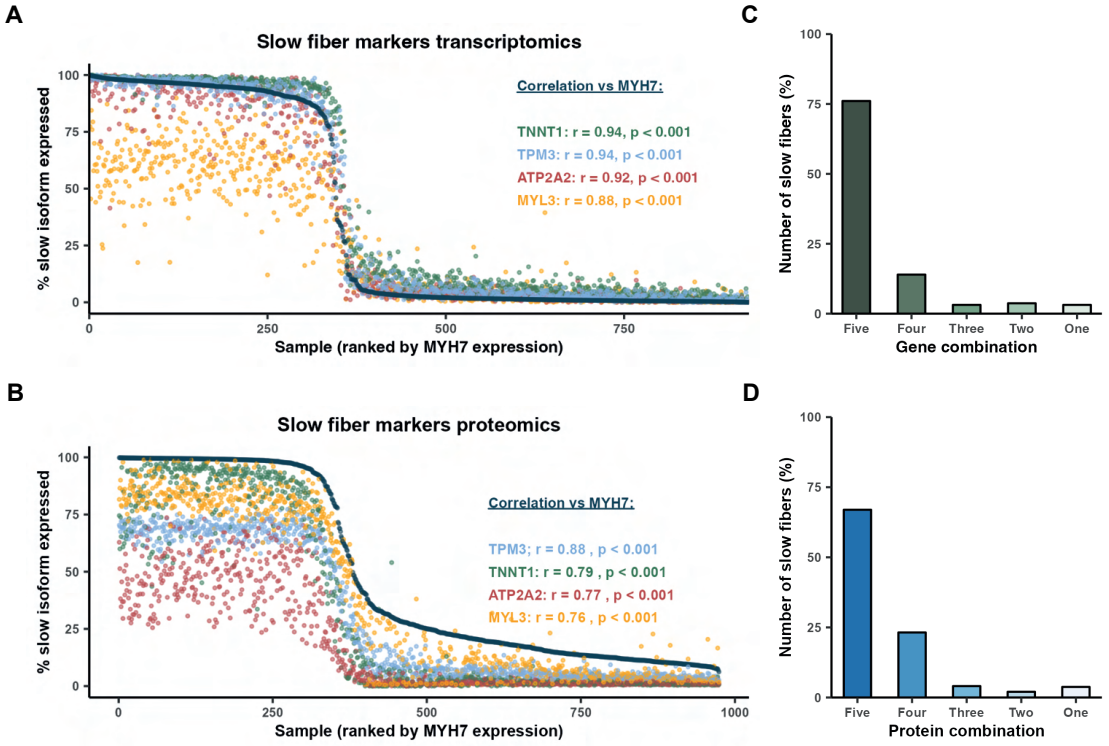

Figure 2 S1. Heterogeneity of fibers with well-known fiber type specific features. (**A-B**) Fiber type curves of established slow fiber type genes/proteins in 1000 fiber transcriptomics and proteomics. (**C-D**) Proportion of fibers determined to be slow via different numerical combinations of genes/proteins in 1000 fiber transcriptomics and proteomics.

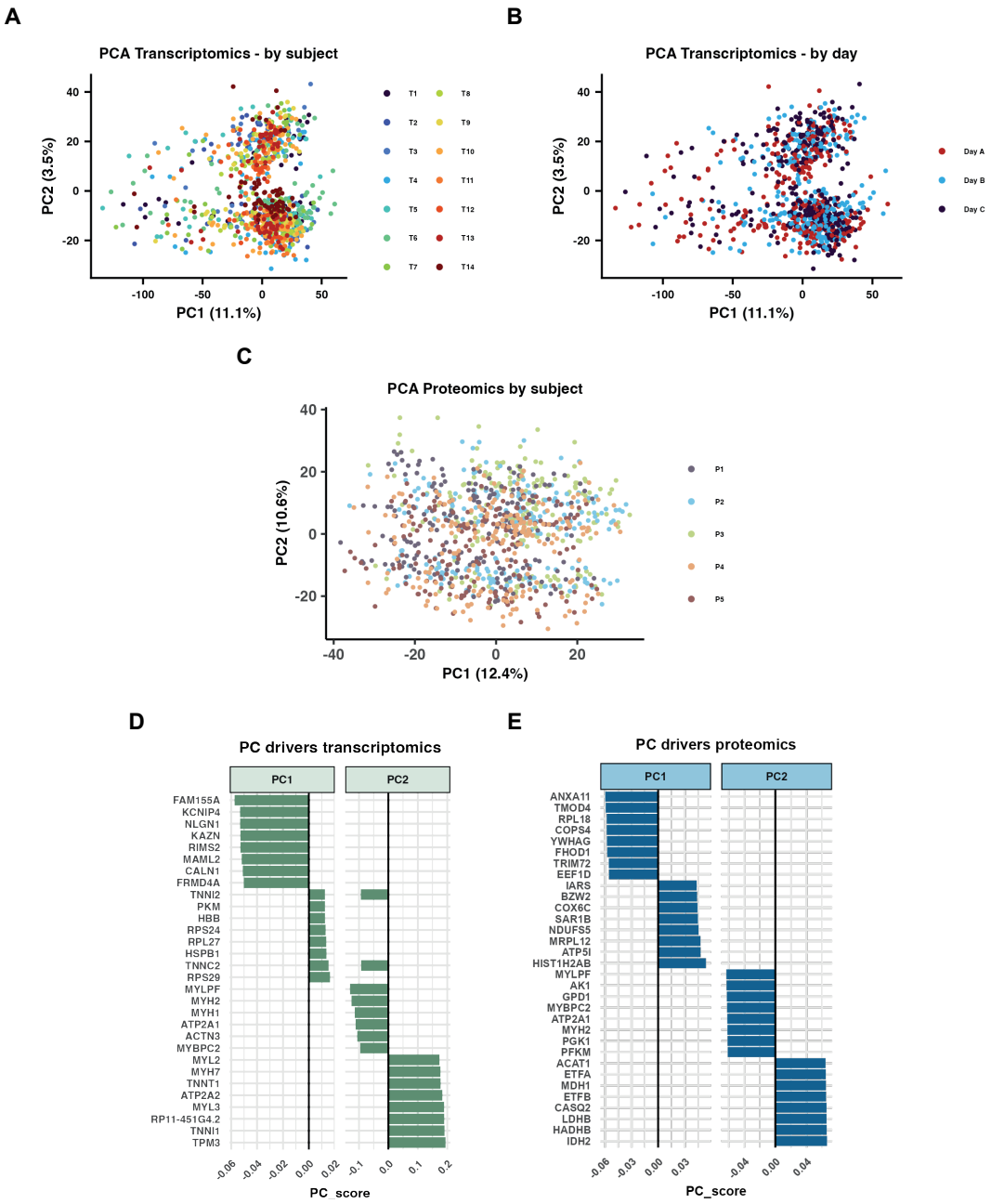

Figure 2 S2. Additional data of Principal Component Analysis (PCA). (**A-B**) 1000 fiber transcriptomics PCA plot colored by participant or trial day. (**C**) 1000 fiber proteomics PCA plot colored by participant. (**D-E**) Top gene and protein drivers of PC1 and PC2**.**

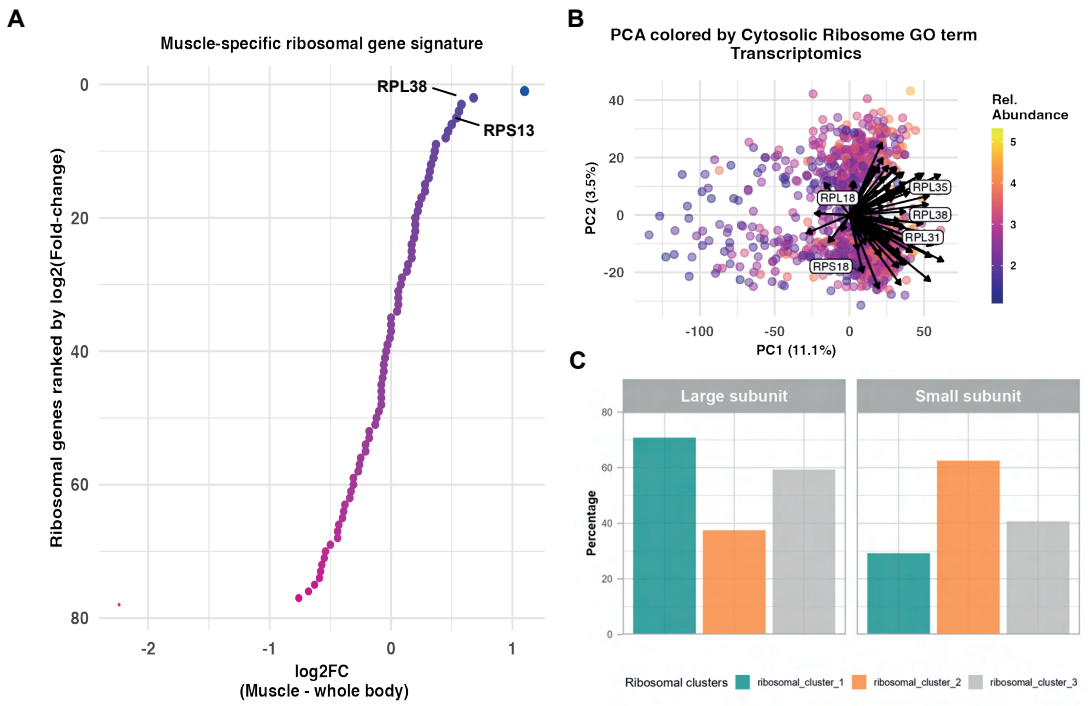

Figure 3 S1. Ribosomal heterogeneity of skeletal muscle fibers. (**A**) mRNA expression of ribosomal proteins in skeletal muscle compared to the whole body. Data derived from Panda et al[67]. (**B**) PCA plot colored by cytosolic ribosome gene ontology (GO) term in the transcriptome. Arrows represent protein drivers and their direction. (**C**) Proportions of ribosomal proteins in each cluster by small (40S) and large (60S) subunits.

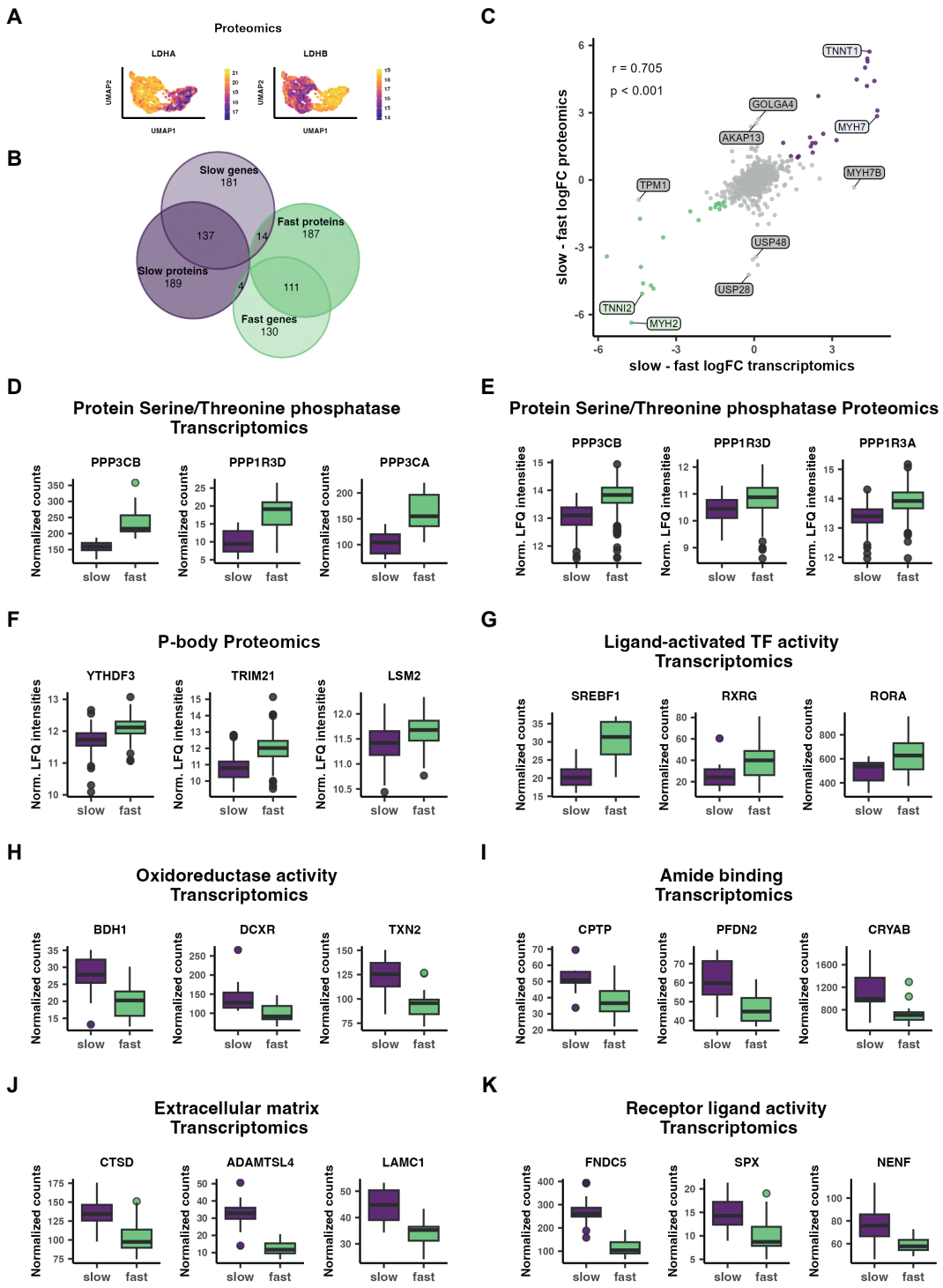

Figure 4 S1. Gene and protein signature of fast and slow fibers. (**A**) Feature plots of LDH protein isoforms between slow and fast fibers. (**B**) Overlap of significantly different genes/proteins between slow and fast skeletal muscle fibers in 1000 fiber transcriptomics and proteomics. (**C**) Correlation between the $\log_2$ fold change difference between slow and fast skeletal muscle fibers within 1000 fiber transcriptomics and proteomics. (**D-K**) Expression profiles of top drivers of selected enrichment terms within slow or fast fibers.

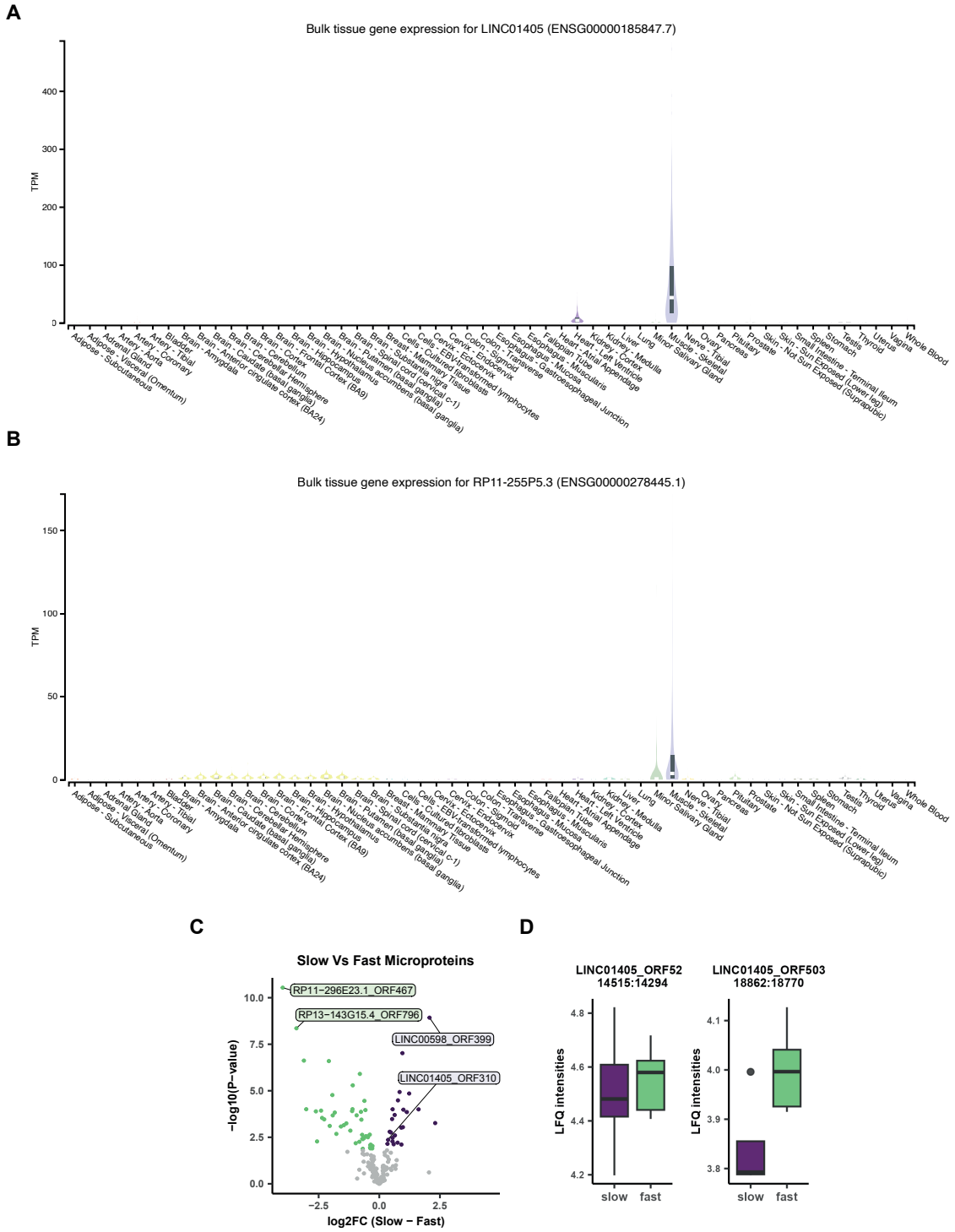

Figure 4 S2. Specific expression of non-coding RNA in skeletal muscle. (**A-B**) Expression profile of *LINC01405* and *RP11-255P5.3* in different tissues. (**C**) Volcano plots comparing microprotein abundance between the slow and fast clusters identified from the uniform manifold approximation and projection (UMAP) plots in Fig 1G-H. Colored dots represent significantly different microproteins at an FDR < 0.05. **(D)** Slow/fast fiber-type comparison of LINC01405_ORF52 14515:14294 and LINC01405_ORF503 18862:18770 microproteins.

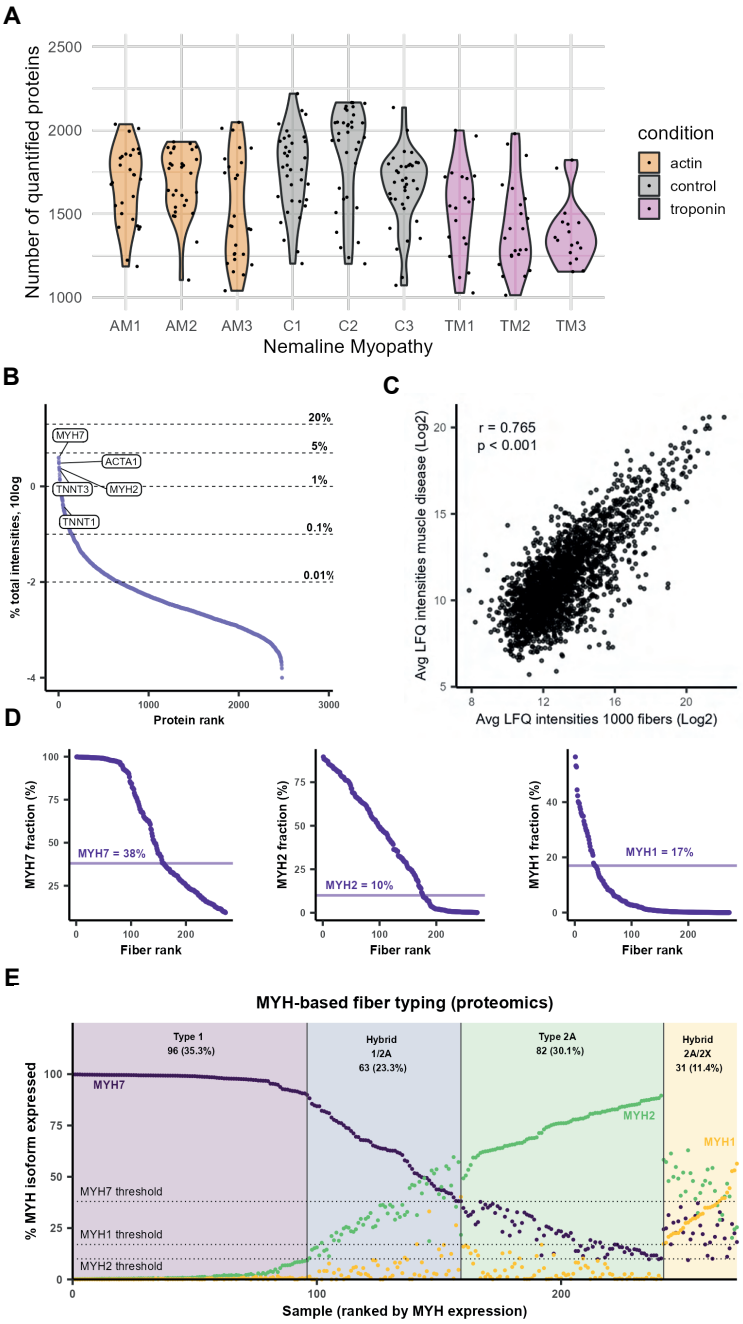

Figure 5 S1. Quality control and fiber typing of nemaline myopathy dataset. (**A**) Number of quantified proteins by participant and sample in nemaline myopathy proteomics. (**B**) Dynamic range of proteins in nemaline myopathy proteomics. (**C**) Correlation between features within 1000 fiber proteomics and healthy controls of nemaline myopathy proteomics. (**D**) Dynamic range curves for MYH7, MYH2, and MYH1, with calculated assignment thresholds. (**E**) Distribution of fibers by expression of MYHs in nemaline myopathy proteomics.

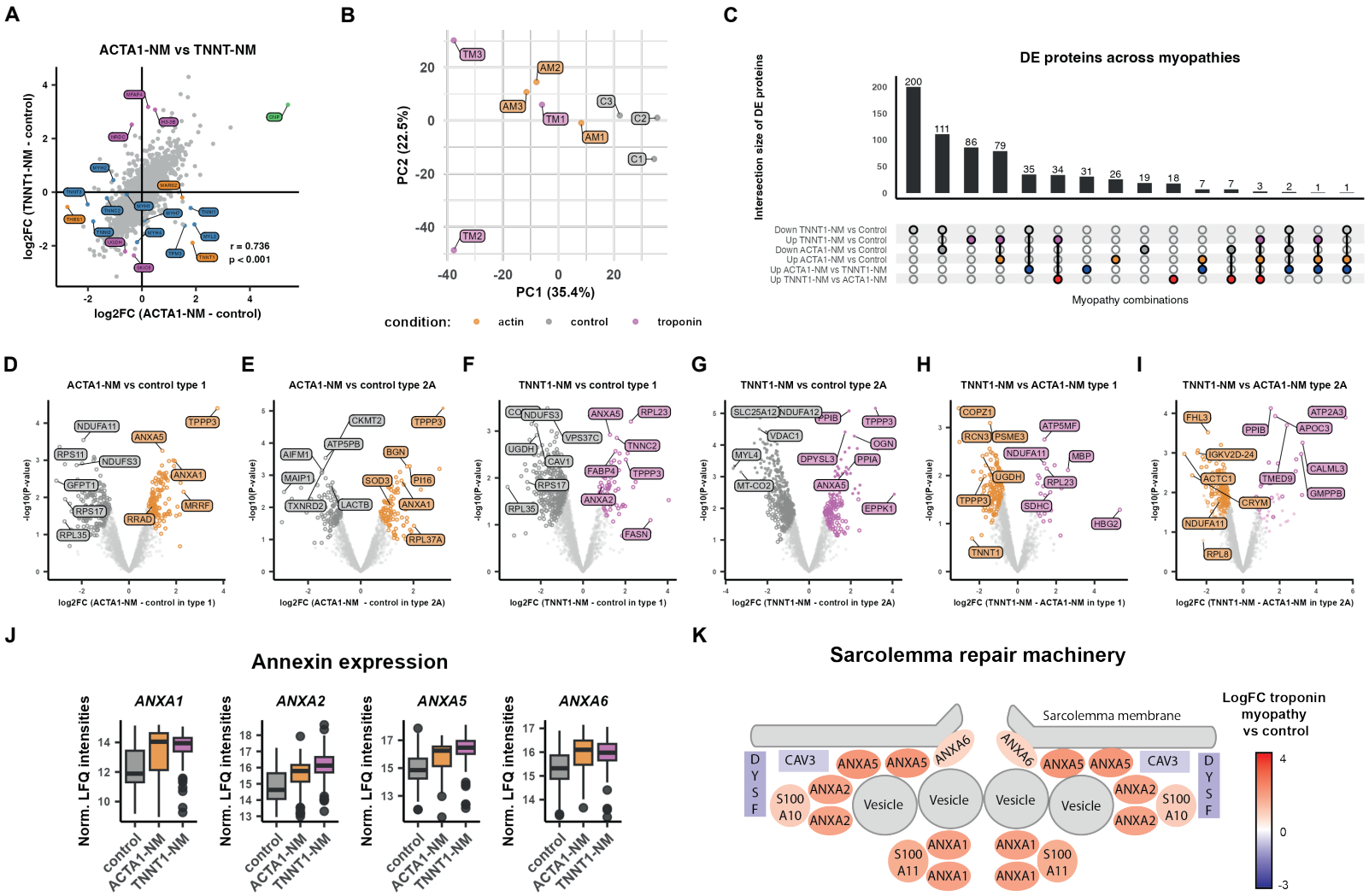

Figure 5 S2. Fiber type-independent remodelling in nemaline myopathy. (**A**) Correlation between the $\log_2$ fold change difference between *ACTA1*- and *TNNT1*-nemaline myopathies with control participants. (**B**) PCA of nemaline myopathy patients (pseudobulked protein profile form single fibers). (**C**) Upset plot of significantly regulated proteins *ACTA1*- and *TNNT1*-nemaline myopathies. (**D-I**) Volcano plots comparing the *ACTA1*- and *TNNT1*-nemaline myopathies with control participants by MYH-based fiber type. (**J**) Abundance of annexin proteins in *ACTA1*- and *TNNT1*-nemaline myopathy. (**K**) Schematic of changes within the sarcolemma repair machinery in nemaline myopathy.

Supplementary Tables

Tables can be accessed here: https://drive.google.com/drive/folders/15j7U-Yj3_2y9bICxouWAhF4yUgXVHBHL

Table S1. Characteristics of participants of the 1000 fiber transcriptomics and proteomics datasets.

Table S2. Raw UMI counts matrix of the 1000 fiber transcriptomics dataset.

Table S3. Raw LFQ intensity matrix of the 1000 fiber proteomics dataset.

Table S4. Quantified transcripts (raw UMI counts) within the 1000 fiber transcriptomics dataset after filtering.

Table S5. Quantified proteins ($\log_2$ LFQ intensity) within the 1000 fiber proteomics dataset after filtering and imputation.

Table S6. Classification system for fiber typing based on myosin heavy chain isoform expression.

Table S7. PC1 and PC2 drivers within the 1000 fiber transcriptomics dataset.

Table S8. PC1 and PC2 drivers within the 1000 fiber proteomics dataset.

Table S9. Over-representation analysis of the top drivers (top 5%) in PC1 and PC2 within the 1000 fiber transcriptomics and proteomics datasets.

Table S10. Protein abundance of proteins within the GO term “Cytosolic Ribosome” in the 1000 fiber proteomics dataset.

Table S11. Pseudobulked transcript expression within slow and fast skeletal muscle fibers in the 1000 fiber transcriptomics dataset.

Table S12. Pseudobulked protein abundance within slow and fast skeletal muscle fibers in the 1000 fiber proteomics dataset.

Table S13. Differential expression results between slow and fast skeletal muscle fibers in the 1000 fiber transcriptomics dataset.

Table S14. Differential abundance results between slow and fast skeletal muscle fibers in the 1000 fiber proteomics dataset.

Table S15. Over-representation analysis of the differentially regulated transcripts and proteins between slow and fast skeletal muscle fibers in the 1000 fiber transcriptomics and proteomics datasets.

Table S16. Transcription factor binding motif enrichment using the TRANSFAC databases on the differentially expressed transcripts between slow and fast fibers in the 1000 fiber transcriptomics dataset.

Table S17. Differential expression results between slow and fast skeletal muscle fibers in non-coding transcripts in the 1000 fiber transcriptomics dataset.

Table S18. Raw LFQ intensity matrix of the microprotein datset.

Table S19. Differential expression results between slow and fast skeletal muscle fibers in the microprotein dataset.

Table S20. Characteristics of patients within the nemaline myopathy proteomics dataset.

Table S21. Detected proteins within the nemaline myopathy proteomics dataset.

Table S22. Quantified proteins within the nemaline myopathy proteomics dataset after filtering and imputation.

Table S23. Pseudobulked protein abundance within the nemaline myopathy proteomics dataset.

Table S24. Differential protein abundance within *ACTA1*- and *TNNT1*-nemaline myopathies.

Table S25. Gene set enrichment analysis of the differential regulation within *ACTA1*- and *TNNT1*-nemaline myopathies.

Table S26. Differential protein abundance within *ACTA1*- and *TNNT1*-nemaline myopathies by MYH-based fiber type.

Table S27. Metadata for the 1000 fiber transcriptomics dataset.

Table S28. Metadata for the 1000 fiber proteomics dataset.

Table S29. Metadata for the nemaline myopathy proteomics dataset.

References

1 Schiaffino, S. & Reggiani, C. Fiber types in mammalian skeletal muscles. *Physiol Rev* **91**, 1447-1531 (2011).

2 Altschuler, S. J. & Wu, L. F. Cellular heterogeneity: do differences make a difference? *Cell* **141**, 559-563 (2010).

3 Engel, W. K. The essentiality of histo- and cytochemical studies of skeletal muscle in the investigation of neuromuscular disease. 1962. *Neurology* **12**, 778-784 (1962).

4 Brooke, M. H. & Kaiser, K. K. Three "myosin adenosine triphosphatase" systems: the nature of their pH lability and sulfhydryl dependence. *J Histochem Cytochem* **18**, 670-672 (1970).

5 Biral, D., Betto, R., Danieli-Betto, D. & Salviati, G. Myosin heavy chain composition of single fibres from normal human muscle. *Biochem J* **250**, 307-308 (1988).

6 Tang, F. *et al.* mRNA-Seq whole-transcriptome analysis of a single cell. *Nat Methods* **6**, 377-382 (2009).

7 Islam, S. *et al.* Characterization of the single-cell transcriptional landscape by highly multiplex RNA-seq. *Genome Res* **21**, 1160-1167 (2011).

8 Brunner, A.-D. *et al.* Ultra-high sensitivity mass spectrometry quantifies single-cell proteome changes upon perturbation. *Mol Syst Biol* **18**, e10798 (2022).

9 Murgia, M. *et al.* Single muscle fiber proteomics reveals fiber-type-specific features of human muscle aging. *Cell Rep* **19**, 2396-2409 (2017).

10 Murgia, M. *et al.* Signatures of muscle disuse in spaceflight and bed rest revealed by single muscle fiber proteomics. *PNAS Nexus* **1**, pgac086 (2022).

11 Murgia, M. *et al.* Single muscle fiber proteomics reveals unexpected mitochondrial specialization. *EMBO rep* **16**, 387-395 (2015).

12 Murgia, M. *et al.* Protein profile of fiber types in human skeletal muscle: a single-fiber proteomics study. *Skeletal Muscle* **11**, 24 (2021).

13 Lang, F. *et al.* Single muscle fiber proteomics reveals distinct protein changes in slow and fast fibers during muscle atrophy. *J Proteome Res* **17**, 3333-3347 (2018).

14 Momenzadeh, A. *et al.* A complete workflow for high throughput human single skeletal muscle fiber proteomics. *J Am Soc Mass Spectrom* (2023).

15 Chemello, F. *et al.* Degenerative and regenerative pathways underlying Duchenne muscular dystrophy revealed by single-nucleus RNA sequencing. *Proc Natl Acad Sci USA* **117**, 29691-29701 (2020).

16 Lin, H. *et al.* Decoding the transcriptome of denervated muscle at single-nucleus resolution. *J Cachexia Sarcopenia Muscle* **13**, 2102-2117 (2022).

17 Sewry, C. A., Laitila, J. M. & Wallgren-Pettersson, C. Nemaline myopathies: a current view. *J Muscle Res Cell Motil* **40**, 111-126 (2019).

18 Laitila, J. & Wallgren-Pettersson, C. Recent advances in nemaline myopathy. *Neuromuscul Disord* **31**, 955-967 (2021).

19 Zhang, M. J., Ntranos, V. & Tse, D. Determining sequencing depth in a single-cell RNA-seq experiment. *Nat Commun* **11**, 774 (2020).

20 Bache, N. *et al.* A novel LC system embeds analytes in pre-formed gradients for rapid, ultra-robust proteomics. *Mol Cell Proteomics* **17**, 2284-2296 (2018).

21 Meier, F. *et al.* diaPASEF: parallel accumulation–serial fragmentation combined with data-independent acquisition. *Nat Methods* **17**, 1229-1236 (2020).

1171 22 Deshmukh, A. S. *et al.* Deep muscle-proteomic analysis of freeze-dried human muscle
1172 biopsies reveals fiber type-specific adaptations to exercise training. *Nat Commun* **12**,
1173 304 (2021).
1174 23 Pardo, J. V., Siliciano, J. D. & Craig, S. W. A vinculin-containing cortical lattice in
1175 skeletal muscle: transverse lattice elements ("costameres") mark sites of attachment
1176 between myofibrils and sarcolemma. *Proc Natl Acad Sci USA* **80**, 1008-1012 (1983).
1177 24 Xiao, Y. *et al.* Loss of mitochondrial protein CHCHD10 in skeletal muscle causes
1178 neuromuscular junction impairment. *Hum Mol Genet* **29**, 1784-1796 (2020).
1179 25 Cho, H. J. *et al.* SLIT3 promotes myogenic differentiation as a novel therapeutic factor
1180 against muscle loss. *J Cachexia Sarcopenia Muscle* **12**, 1724-1740 (2021).
1181 26 Han, S. *et al.* Nuclear envelope phosphatase 1-regulatory subunit 1 (formerly
1182 TMEM188) is the metazoan Spo7p ortholog and functions in the lipin activation
1183 pathway. *J Biol Chem* **287**, 3123-3137 (2012).
1184 27 Hengel, H. *et al.* Loss-of-function mutations in UDP-Glucose 6-Dehydrogenase cause
1185 recessive developmental epileptic encephalopathy. *Nat Commun* **11**, 595 (2020).
1186 28 Farhang-Fallah, J. *et al.* The pleckstrin homology (PH) domain-interacting protein
1187 couples the insulin receptor substrate 1 PH domain to insulin signaling pathways
1188 leading to mitogenesis and GLUT4 translocation. *Mol Cell Biol* **22**, 7325-7336 (2002).
1189 29 Genuth, N. R. & Barna, M. The discovery of ribosome heterogeneity and its
1190 implications for gene regulation and organismal life. *Mol Cell* **71**, 364-374 (2018).
1191 30 Parks, M. M. *et al.* Variant ribosomal RNA alleles are conserved and exhibit tissue-
1192 specific expression. *Sci Adv* **4**, eaao0665 (2018).
1193 31 Slavov, N., Semrau, S., Airoldi, E., Budnik, B. & van Oudenaarden, A. Differential
1194 stoichiometry among core ribosomal proteins. *Cell Rep* **13**, 865-873 (2015).
1195 32 Shi, Z. *et al.* Heterogeneous ribosomes preferentially translate distinct subpools of
1196 mRNAs genome-wide. *Mol Cell* **67**, 71-83.e77 (2017).
1197 33 Kondrashov, N. *et al.* Ribosome-mediated specificity in Hox mRNA translation and
1198 vertebrate tissue patterning. *Cell* **145**, 383-397 (2011).
1199 34 Genuth, N. R. *et al.* A stem cell roadmap of ribosome heterogeneity reveals a
1200 function for RPL10A in mesoderm production. *Nat Commun* **13**, 5491 (2022).
1201 35 Landry, D. M., Hertz, M. I. & Thompson, S. R. RPS25 is essential for translation
1202 initiation by the Dicistroviridae and hepatitis C viral IRESs. *Genes Dev* **23**, 2753-2764
1203 (2009).
1204 36 Horos, R. *et al.* Ribosomal deficiencies in Diamond-Blackfan anemia impair
1205 translation of transcripts essential for differentiation of murine and human
1206 erythroblasts. *Blood* **119**, 262-272 (2012).
1207 37 Anger, A. M. *et al.* Structures of the human and Drosophila 80S ribosome. *Nature*
1208 **497**, 80-85 (2013).
1209 38 Spahn, C. M. *et al.* Cryo-EM visualization of a viral internal ribosome entry site bound
1210 to human ribosomes: the IRES functions as an RNA-based translation factor. *Cell* **118**,
1211 465-475 (2004).
1212 39 Boehringer, D., Thermann, R., Ostareck-Lederer, A., Lewis, J. D. & Stark, H. Structure
1213 of the hepatitis C virus IRES bound to the human 80S ribosome: Remodeling of the
1214 HCV IRES. *Structure* **13**, 1695-1706 (2005).
1215 40 Kannan, K., Vázquez-Laslop, N. & Mankin, A. S. Selective protein synthesis by
1216 ribosomes with a drug-obstructed exit tunnel. *Cell* **151**, 508-520 (2012).

41 Armstrong, E. *et al.* Comparison of transcriptomic landscapes of different lamb muscles using RNA-Seq. *PLoS One* **13**, e0200732 (2018).
42 Leberer, E. & Pette, D. Lactate dehydrogenase isozymes in type I, IIA and IIB fibres of rabbit skeletal muscles. *Histochemistry* **80**, 295-298 (1984).
43 Rubenstein, A. B. *et al.* Single-cell transcriptional profiles in human skeletal muscle. *Sci Rep* **10**, 229 (2020).
44 Lerín, C. *et al.* Regulation and function of the muscle glycogen-targeting subunit of protein phosphatase 1 (GM) in human muscle cells depends on the COOH-terminal region and glycogen content. *Diabetes* **52**, 2221-2226 (2003).
45 Luo, Y., Na, Z. & Slavoff, S. A. P-bodies: Composition, properties, and functions. *Biochemistry* **57**, 2424-2431 (2018).
46 Chin, E. R. *et al.* A calcineurin-dependent transcriptional pathway controls skeletal muscle fiber type. *Genes Dev* **12**, 2499-2509 (1998).
47 Kammoun, M. *et al.* Novel role of Tieg1 in muscle metabolism and mitochondrial oxidative capacities. *Acta Physiologica* **228**, e13394 (2020).
48 Statello, L., Guo, C.-J., Chen, L.-L. & Huarte, M. Gene regulation by long non-coding RNAs and its biological functions. *Nat Rev Mol Cell Biol* **22**, 96-118 (2021).
49 Lorenzi, L. *et al.* The RNA Atlas expands the catalog of human non-coding RNAs. *Nat Biotech* **39**, 1453-1465 (2021).
50 Wang, W. *et al.* Identification of miRNA, lncRNA and mRNA-associated ceRNA networks and potential biomarker for MELAS with mitochondrial DNA A3243G mutation. *Sci Rep* **7**, 41639 (2017).
51 Volders, P.-J. *et al.* LNCipedia 5: towards a reference set of human long non-coding RNAs. *Nucleic Acids Res* **47**, D135-D139 (2019).
52 Matsumoto, A. *et al.* mTORC1 and muscle regeneration are regulated by the LINC00961-encoded SPAR polypeptide. *Nature* **541**, 228-232 (2017).
53 Nelson, B. R. *et al.* A peptide encoded by a transcript annotated as long noncoding RNA enhances SERCA activity in muscle. *Science* **351**, 271-275 (2016).
54 Bittel, D. C. *et al.* Annexin A2 mediates dysferlin accumulation and muscle cell membrane repair. *Cells* **9** (2020).
55 Carmeille, R. *et al.* Membrane repair of human skeletal muscle cells requires Annexin-A5. *Biochim Biophys Acta* **1863**, 2267-2279 (2016).
56 Jaiswal, J. K. *et al.* S100A11 is required for efficient plasma membrane repair and survival of invasive cancer cells. *Nat Commun* **5**, 3795 (2014).
57 Cagliani, R. *et al.* Mutation finding in patients with dysferlin deficiency and role of the dysferlin interacting proteins annexin A1 and A2 in muscular dystrophies. *Hum Mutat* **26**, 283 (2005).
58 Leikina, E. *et al.* Extracellular annexins and dynamin are important for sequential steps in myoblast fusion. *J Cell Biol* **200**, 109-123 (2012).
59 Zhu, B. *et al.* Monoubiquitination of human histone H2B: the factors involved and their roles in HOX gene regulation. *Mol Cell* **20**, 601-611 (2005).
60 Needham, D. M. Red and white muscle. *Physiol Revs* **6**, 1-27 (1926).
61 Petrany, M. J. *et al.* Single-nucleus RNA-seq identifies transcriptional heterogeneity in multinucleated skeletal myofibers. *Nat Commun* **11**, 6374 (2020).
62 Musalgaonkar, S., Black, J. J. & Johnson, A. W. The L1 stalk is required for efficient export of nascent large ribosomal subunits in yeast. *Rna* **25**, 1549-1560 (2019).

63 Fernández, I. S., Bai, X. C., Murshudov, G., Scheres, S. H. & Ramakrishnan, V. Initiation of translation by cricket paralysis virus IRES requires its translocation in the ribosome. *Cell* **157**, 823-831 (2014).
64 Turner, D. C. *et al.* DNA methylation across the genome in aged human skeletal muscle tissue and muscle-derived cells: the role of HOX genes and physical activity. *Sci Rep* **10**, 15360 (2020).
65 Robinson, M. M. *et al.* Enhanced protein translation underlies improved metabolic and physical adaptations to different exercise training modes in young and old humans. *Cell Metab* **25**, 581-592 (2017).
66 D'Ercole, C. *et al.* Spatially resolved transcriptomics reveals innervation-responsive functional clusters in skeletal muscle. *Cell Rep* **41**, 111861 (2022).
67 Fitzgerald, G. *et al.* MME+ fibro-adipogenic progenitors are the dominant adipogenic population during fatty infiltration in human skeletal muscle. *Commun Biol* **6**, 111 (2023).
68 Babaeijandaghi, F. *et al.* Metabolic reprogramming of skeletal muscle by resident macrophages points to CSF1R inhibitors as muscular dystrophy therapeutics. *Sci Trans Med* **14**, eabg7504 (2022).
69 Chaillou, T., Zhang, X. & McCarthy, J. J. Expression of Muscle-Specific Ribosomal Protein L3-Like Impairs Myotube Growth. *J Cell Physiol* **231**, 1894-1902 (2016).
70 Seaborne, R. A. E. & Ochala, J. The dawn of the functional genomics era in muscle physiology. *J Physiol* **601**, 1343-1352 (2023).
71 Van der Stede, T. *et al.* Histamine H(1) and H(2) receptors are essential transducers of the integrative exercise training response in humans. *Sci Adv* **7** (2021).
72 Bergström, J. Percutaneous needle biopsy of skeletal muscle in physiological and clinical research. *Scand J Clin Lab Invest* **35**, 609-616 (1975).
73 Hao, Y. *et al.* Integrated analysis of multimodal single-cell data. *Cell* **184**, 3573-3587.e3529 (2021).
74 Choudhary, S. & Satija, R. Comparison and evaluation of statistical error models for scRNA-seq. *Genome Biol* **23**, 27 (2022).
75 Sahl, R. E. *et al.* Variation in mitochondrial respiratory capacity and myosin heavy chain composition in repeated muscle biopsies. *Anal Biochem* **556**, 119-124 (2018).
76 Ranu, N. *et al.* NEB mutations disrupt the super-relaxed state of myosin and remodel the muscle metabolic proteome in nemaline myopathy. *Acta Neuropathol Commun* **10**, 185 (2022).
77 Demichev, V. *et al.* dia-PASEF data analysis using FragPipe and DIA-NN for deep proteomics of low sample amounts. *Nat Commun* **13**, 3944 (2022).
78 Demichev, V., Messner, C. B., Vernardis, S. I., Lilley, K. S. & Ralser, M. DIA-NN: neural networks and interference correction enable deep proteome coverage in high throughput. *Nat Methods* **17**, 41-44 (2020).
79 Ritchie, M. E. *et al.* LIMMA powers differential expression analyses for RNA-sequencing and microarray studies. *Nucleic Acids Res* **43**, e47 (2015).
80 Müller, C. *et al.* Removing batch effects from longitudinal gene expression - Quantile normalization plus ComBat as best approach for microarray transcriptome data. *PLoS One* **11**, e0156594 (2016).
81 Kim, H. J. *et al.* PhosR enables processing and functional analysis of phosphoproteomic data. *Cell Rep* **34**, 108771 (2021).

82 Wu, T. *et al.* clusterProfiler 4.0: A universal enrichment tool for interpreting omics data. *Innovation (Camb)* **2**, 100141 (2021).
83 Love, M. I., Huber, W. & Anders, S. Moderated estimation of fold change and dispersion for RNA-seq data with DESeq2. *Genome Biol* **15**, 550 (2014).
84 Xiao, Y. *et al.* A novel significance score for gene selection and ranking. *Bioinformatics* **30**, 801-807 (2014).
85 Panda, A. *et al.* Tissue- and development-stage–specific mRNA and heterogeneous CNV signatures of human ribosomal proteins in normal and cancer samples. *Nucleic Acids Res* **48**, 7079-7098 (2020).
86 Pettersen, E. F. *et al.* UCSF ChimeraX: Structure visualization for researchers, educators, and developers. *Protein Sci* **30**, 70-82 (2021).